

# On the amplification of magnetic fields in cosmic filaments and galaxy clusters\*

F. Vazza,<sup>1,2†</sup> M. Brüggen,<sup>1</sup> C. Gheller<sup>3</sup> and P. Wang<sup>4</sup>

<sup>1</sup>Hamburger Sternwarte, Gojenbergsweg 112, D-21029 Hamburg, Germany

<sup>2</sup>INAF/Istituto di Radioastronomia, via Gobetti 101, I-40129 Bologna, Italy

<sup>3</sup>CSCS, Via Trevano 131, CH-6900 Lugano, Switzerland

<sup>4</sup>NVIDIA, Santa Clara, 95050, USA

Accepted 2014 September 9. Received 2014 September 8; in original form 2014 September 2

## ABSTRACT

The amplification of primordial magnetic fields via a small-scale turbulent dynamo during structure formation might be able to explain the observed magnetic fields in galaxy clusters. The magnetization of more tenuous large-scale structures such as cosmic filaments is more uncertain, as it is challenging for numerical simulations to achieve the required dynamical range. In this work, we present magnetohydrodynamical cosmological simulations on large uniform grids to study the amplification of primordial seed fields in the intracluster medium (ICM) and in the warm–hot–intergalactic medium (WHIM). In the ICM, we confirm that turbulence caused by structure formation can produce a significant dynamo amplification, even if the amplification is smaller than what is reported in other papers. In the WHIM inside filaments, we do not observe significant dynamo amplification, even though we achieve Reynolds numbers of  $R_e \sim 200$ –300. The maximal amplification for large filaments is of the order of  $\sim 100$  for the magnetic energy, corresponding to a typical field of a few  $\sim \text{nG}$  starting from a primordial weak field of  $10^{-10}$  G (comoving). In order to start a small-scale dynamo, we found that a minimum of  $\sim 10^2$  resolution elements across the virial radius of galaxy clusters was necessary. In filaments we could not find a minimum resolution to set off a dynamo. This stems from the inefficiency of supersonic motions in the WHIM in triggering solenoidal modes and small-scale twisting of magnetic field structures. Magnetic fields this small will make it hard to detect filaments in radio observations.

**Key words:** methods: numerical – intergalactic medium – large-scale structure of Universe.

## 1 INTRODUCTION

Cosmic magnetism is an astrophysical puzzle. While radio observations provide evidence for magnetic field strengths of up to a few  $\sim \mu\text{G}$  in galaxy clusters and galaxies (e.g. Ferrari et al. 2008; Brüggen et al. 2011; Ryu et al. 2012, and references therein), the origin of such strong fields is unclear, given that the upper limits on the primordial magnetic field at the epoch of the cosmic microwave background set  $B < 10^{-10}$  G (e.g. Neronov & Vovk 2010).

From a theoretical point of view, the first cosmic seed fields can be generated in the very early Universe during inflation and first-order phase transitions (however, the uncertainty on the efficiency of such mechanisms is large,  $B \sim 10^{-34}$ – $10^{-10}$  G; e.g. Widrow et al. 2012). Additional processes such as the Biermann-battery, or aperiodic

turbulent fluctuations in the intergalactic plasma, might also provide seed fields in the range  $\sim 10^{-19}$ – $10^{-16}$  G (Kulsrud et al. 1997; Schlickeiser 2012). Later on, structure formation can cause further amplification via a small-scale turbulent dynamo (e.g. Subramanian, Shukurov & Haugen 2006) in two main phases: first, via exponential growth of the magnetic field in the kinematic regime, and, secondly, via non-linear growth and stretching of the coherence scales until saturation with the turbulent forcing (Wang & Abel 2009; Beck et al. 2012; Schober, Schleicher & Klessen 2013; Pakmor, Marinacci & Springel 2014). Galactic activity can yield localized additional seeding (e.g. Kronberg, Lesch & Hopp 1999; Völk & Atoyan 2000), while further amplification in cluster outskirts might be produced via the magnetothermal instability (Parrish, Stone & Lemaster 2008) or instabilities driven by cosmic rays accelerated by shocks (Drury & Downes 2012; Brüggen 2013). At higher redshifts ( $z \sim 2$ ), star formation should be able to induce small-scale dynamo by injecting turbulence from supernova explosions (e.g. Beck et al. 1996, 2013), producing large rotation measures (e.g. Kronberg et al. 2008; Mao et al. 2012) and possibly explaining the tight correlation between far-infrared and radio continuum emission (Schleicher & Beck 2013).

\* F. V. would like to dedicate this paper to the memory of Piero Pasini, who recently passed away, former president of Associazione Astrofili Vittorio Veneto, an old friend and inspirational figure in F.V.’s career.

† E-mail: [franco.vazza@hs.uni-hamburg.de](mailto:franco.vazza@hs.uni-hamburg.de)

Cosmological simulations can reproduce the observed field strengths within galaxies and galaxy clusters starting from weak primordial fields (e.g. Dolag, Bartelmann & Lesch 1999; Brüggen et al. 2005; Bonafede et al. 2011; Ruszkowski et al. 2011), yet similar field strengths can also be achieved with outflows from active galactic nuclei (e.g. Dubois & Teyssier 2008; Xu et al. 2009), galactic winds (e.g. Donnert et al. 2009) and star formation (e.g. Beck et al. 2013). In particular, Donnert et al. (2009) concluded that magnetized galactic outflows and their subsequent evolution within the intracluster medium (ICM) in principle can explain the observed magnetization of galaxy clusters, while measuring cosmological magnetic fields in low-density environments can reveal the origin of cosmic magnetic fields.

Very little is known about the evolution and present-day distribution of magnetic fields in the periphery of galaxy clusters and in the cosmic web, particularly in filaments that contain  $\sim 50$ –60 per cent of the total mass in the Universe (e.g. Cautun et al. 2014). This circumstance makes the study of ultrahigh energy cosmic rays (UHECRs) very uncertain since large-scale magnetic fields change the arrival direction of UHECRs (e.g. Sigl, Miniati & Ensslin 2003; Ryu, Das & Kang 2010). This also adds uncertainties to the composition of UHECRs, as the presence of magnetic fields can significantly alter the spectrum and composition of UHECRs that reach Earth (e.g. Alves Batista, Schiffer & Sigl 2014).

Numerical simulations are crucial for studying the non-linear processes that lead to the amplification of the seed magnetic fields during structure formation. In simulations, a large spatial resolution is needed to produce the degree of turbulence that leads to dynamo amplification (e.g. Federrath et al. 2011a; Turk et al. 2012; Latif et al. 2013). However, in filaments, neither Lagrangian (such as smooth particle hydrodynamics) nor mesh refinement schemes based on matter density, achieve the necessary resolution. On the other hand, the use of fixed grids is computationally demanding due to the need of resolving the details of the internal structure of filaments. Whether the magnetic field in filaments approaches equipartition with the kinetic energy, is unclear. The amplification is expected to depend on the numerical resolution, on the exact distribution of modes (compressive or solenoidal), as well as on the range of dynamical scales (Schekochihin et al. 2004; Ryu et al. 2008; Cho et al. 2009; Jones et al. 2011).

Modelling of magnetic fields in filaments is relevant for the study of radio emission from the cosmic web, that surveys in the nearby (e.g. Low-Frequency Array [LOFAR]) and more distant future (e.g. the Square Kilometer Array [SKA]) might be able to detect for the first time, in case of large enough magnetic fields (Brown 2011; Araya-Melo et al. 2012).

## 2 METHODS

### 2.1 ENZO-MHD

The simulations performed in this work have been produced with a customized version of the grid code ENZO (Bryan G. L. et al. [The Enzo Collaboration], 2014). ENZO is a highly parallel code for cosmological magnetohydrodynamics (MHD), which uses a particle-mesh  $N$ -body method (PM) to follow the dynamics of the dark matter (DM) and a variety of shock-capturing Riemann solvers to evolve the gas component.

The MHD implementation of ENZO that we use has been developed by Wang & Abel (2009) and Wang, Abel & Kaehler (2010). It is based on the Dedner formulation of MHD equations (Dedner et al. 2002), which uses hyperbolic divergence cleaning to pre-

serve the  $\nabla \cdot \mathbf{B} = 0$  condition. The MHD solver adopted here uses a piecewise-linear reconstruction, where fluxes at cell interfaces are calculated using the Harten-Lax-van Leer (HLL) approximate Riemann solver (Harten & Hyman 1983) and time integration is performed using a total variation diminishing second-order Runge–Kutta scheme (Shu & Osher 1988). The resulting solver is expected to be slightly more diffusive than the piecewise-parabolic approach, but allows a more efficient treatment of the electromagnetic terms. Extensive tests have been conducted to compare the performance of different MHD solvers in astrophysical codes (including the implementation of the Dedner scheme employed here) in the case of decaying supersonic turbulence. Overall, the Dedner cleaning compared well with more complex MHD schemes, at the price of being more dissipative at very small spatial scales, due to the small-scale  $\nabla \cdot \mathbf{B}$  waves generated by this scheme (Kritsuk et al. 2011). For further tests on the validation of the code we refer the reader to Wang & Abel (2009).

This MHD solver, as well as a version of the Piecewise Parabolic Method (PPM) hydro solver, has been ported to NVIDIA’s CUDA framework, allowing ENZO to take advantage of modern graphics hardware (Wang et al. 2010; Bryan G. L. et al. [The Enzo Collaboration], 2014). A key step in ENZO’s implementation is flux correction, which is required when each level of resolution is allowed to take its own time step. Within the GPU version of the MHD solvers, the fluxes are calculated on the GPU and only the fluxes required for flux correction are transferred back to the CPU. This procedure reduces the overhead associated with the data transfer, which can be large in a heterogeneous architecture of this sort. Due to the explicit, directionally split stencil pattern of both the PPM and Dedner MHD solvers, they are well suited for hardware acceleration. The porting on to GPUs replaced many shared temporary arrays of the CPU version into larger temporary arrays that are not shared among loop iterations, and exposed the massive parallelism in the algorithm using CUDA. For further details on the porting on to CUDA, we refer the reader to Wang et al. (2010) and Bryan G. L. et al. (The Enzo Collaboration), 2014.

Most of our simulations were run on the Piz Daint system (deployed by ETHZ CSCS Swiss national supercomputing centre in Lugano,<sup>1</sup> a Cray XC30 supercomputer accounting for more than 5000 computing nodes, each equipped with an 8-core 64-bit Intel SandyBridge CPU (Intel Xeon E5-2670) and an NVIDIA Tesla K20X GPU. When running at fixed mesh resolution, the GPU allow to gain a factor of  $\sim 4$  in performance, compared to the usage of the corresponding CPU, reducing accordingly the necessary computing time and allowing the investigation of a larger parameters space, with a given amount of computational resources.

In the appendix, we present a number of tests performed using the CUDA implementation of ENZO’s MHD solver, where we simulated the amplification of a weak uniform field in a cubic box with a steady driving of turbulence.

### 2.2 Setups

We assume a *Wilkinson Microwave Anisotropy Probe* 7-year cosmology with  $\Omega_0 = 1.0$ ,  $\Omega_B = 0.0455$ ,  $\Omega_{\text{DM}} = 0.2265$ ,  $\Omega_{\Lambda} = 0.728$ , Hubble parameter  $h = 0.702$ , and a spectral index of  $n_s = 0.961$  for the primordial spectrum of initial matter fluctuations (Komatsu et al. 2011). The amplitude of the variance of the cosmic spectrum of density at the start of each run has been varied from run to run

<sup>1</sup>[http://www.cscs.ch/computers/piz\\_daint/index.html](http://www.cscs.ch/computers/piz_daint/index.html)

**Table 1.** Main parameters of our MHD runs of a galaxy cluster (with exaggerated  $\sigma_8$ ), employed in Section 3.1. Column 1: number of grid(s) cells in the initial conditions; column 2: spatial resolution; column 3: dark matter mass resolution.

| $N_{\text{grid}}$ | $\Delta x$ (kpc) | $m_{\text{DM}} (M_{\odot} h^{-1})$ |
|-------------------|------------------|------------------------------------|
| $64^3$            | 220              | $2.9 \times 10^8$                  |
| $128^3$           | 110              | $3.6 \times 10^7$                  |
| $256^3$           | 55               | $4.5 \times 10^6$                  |
| $512^3$           | 27               | $5.6 \times 10^5$                  |
| $640^3$           | 22               | $2.9 \times 10^5$                  |
| $1024^3$          | 13               | $7.0 \times 10^4$                  |

as explained in Section 3.1–3.3. The magnetic field in all runs has been initialized to the reference value of  $B_0 = 10^{-10}$  G (comoving), which we imposed as a background uniform field at the beginning of each run. A list of runs is given in Table 1.

### 3 RESULTS

#### 3.1 Magnetic field amplification in the ICM

In a first set of simulations, we measured the amplification of a cosmological weak magnetic field during the formation of a galaxy cluster, as a benchmark test for our following studies of amplification within filaments with ENZO-MHD.

This magnetization of the ICM during structure formation has already been studied with a variety of codes by many authors (e.g. Dolag et al. 1999; Brüggen et al. 2005; Dubois & Teyssier 2008; Xu et al. 2009; Collins et al. 2010; Bonafede et al. 2011), which demonstrated how the amplification of magnetic field is a natural process within the large overdensity of galaxy clusters (even if the amplification factors can change from simulation to simulation). Here, we want to study the growth of magnetic fields as a function of spatial resolution. Hence, we want to limit as much as possible the uncertainties related to the use of adaptive mesh refinement (AMR; e.g. Xu et al. 2009). Therefore, we only used runs with uniform spatial resolution along the whole cluster evolution. To this end, we adopted an artificially large normalization of the primordial matter power spectrum,  $\sigma_8 = 5.0$ , in creating our initial conditions, in order to enable the formation of a single cluster of mass  $\sim 10^{14} M_{\odot}$  even within the rather small volume of (14 Mpc)<sup>3</sup>. Of course, this unrealistically large value of  $\sigma_8$  (to be compared with the concordance value  $\sigma_8 \approx 0.8$ ) will shed little light on the timing of the amplification since a large value of  $\sigma_8$  causes the formation of clusters already at high redshifts. Using this idealized setup, we simulated the evolution of the ICM employing grids from  $64^3$  to  $1024^3$  cells/DM particles corresponding to a comoving spatial resolution from 220 to 13 kpc. A list of our cluster runs is given in Table 1.

Fig. 1 shows maps of temperature and magnetic fields for a slice through the centre of the cluster at  $z = 0$ , for all resolutions from  $64^3$  to  $1024^3$ . While the temperature distribution of the cluster varies slightly across runs, the spatial distribution of the magnetic fields changes clearly with increasing resolution. Starting at a resolution of 27 kpc ( $512^3$ ), the morphology of the magnetic field becomes increasingly more tangled on scales smaller than the cluster core radius, and clumps of gas with  $B \geq 0.1 \mu\text{G}$  start to appear throughout

the virial volume. At our best resolution, the maximum Reynolds number within the virial volume is

$$R_e \approx \left( \frac{2R_v}{2\Delta x} \right)^{4/3} \approx 1400, \quad (1)$$

where  $R_v = 1.5$  Mpc is the virial radius at  $z = 0$  (e.g. Vazza et al. 2011b) and  $\Delta x$  is our (comoving) spatial resolution (13 kpc in the most resolved run). According to simulations of forced turbulence in a box (Schekochihin et al. 2004; Cho et al. 2009; Jones et al. 2011), this is large enough to start a small-scale dynamo. The former likely represents an overestimate of the real Reynolds number in the flow, because the cluster's virial radius was smaller in the past, and because the driving of the turbulence by subclusters preferentially occurs on scales smaller than the current virial radius (Vazza, Roediger & Brueggen 2012), thereby limiting the outer scale of turbulence.

At all resolutions, the radial profile of the magnetic fields at  $z = 0$  (Fig. 2) shows the build-up of the magnetic field in the centre. The growth of the field proceeds faster with increasing resolution in the innermost regions. Inside the virial volume, the average profile of the magnetic field does not vary much with resolution in the range between 27 and 13 kpc, suggesting that we are not far from convergence. The maximum field we observe in the centre is  $\sim 0.7 \mu\text{G}$ , corresponding to a maximum amplification factor of  $\sim 5 \times 10^7$  for the magnetic energy and 7000 for the magnetic field. Beyond the virial radius the simulation does not seem to be fully converged. At distances of  $1R_v$  from the cluster centre, the average field varies from  $\sim 0.02$ – $0.04 \mu\text{G}$  at low resolution to  $\sim 0.1 \mu\text{G}$  at high resolution. For a cluster of this mass and central temperature ( $\sim 3 \times 10^7$  K), the resulting plasma beta is of the order of  $\beta \sim 100$  (where  $\beta = nk_B T / P_B$ , where  $n$  is the gas density and  $P_B$  is the magnetic pressure) in the innermost cluster regions. This matches observations for real galaxy clusters (Murgia et al. 2004; Bonafede et al. 2010).

Fig. 3 shows the comoving kinetic energy per unit mass (top lines) and magnetic field spectra (lower lines) for all resolutions at  $z = 0$ . All spectra were computed in a (7 Mpc)<sup>3</sup> cubic box centred on the cluster, using an FFT algorithm and assuming periodic boundary conditions. In order to compare our spectra to standard ‘turbulence in a box’ simulations (e.g. Haugen, Brandenburg & Dobler 2003; Schekochihin et al. 2004; Cho et al. 2009; Kritsuk et al. 2011), we assumed  $\rho = 1$  for the gas, which removes the effect of density fluctuations on the kinetic energy spectra. The specific kinetic energy spectra are very similar at all resolutions, with a power law slightly steeper than the Kolmogorov slope across more than two orders of magnitude in scale. This is in agreement with previous numerical results (e.g. Vazza et al. 2009, 2011b, 2012; Gaspari & Churazov 2013). The magnetic field spectra, however, show the clear build-up of the small-scale magnetic field as soon as the spatial resolution is sufficiently fine. From  $k \geq 4$ , the magnetic spectra get shallower as resolution is increased, and in the range  $10 \leq k \leq 100$  a significant pile-up of magnetic energy occurs for resolutions better than  $256^3$  (i.e.  $\Delta x \leq 55$  kpc). The observed small-scale spectra are qualitatively similar to previous results by Xu et al. (2009), even if their seeding model for the magnetic field differs from that we adopted. No developed power-law spectra is observed for the magnetic field, but a peak that moves towards larger scales as resolution is increased, similar to Haugen et al. (2003); Cho et al. (2009) and at odds with what is usually assumed in Faraday rotation models (Murgia et al. 2004; Bonafede et al. 2010, 2013). The peak in the magnetic energy is located at  $k \sim 100$  ( $\sim 50$  kpc) in our highest resolution run.

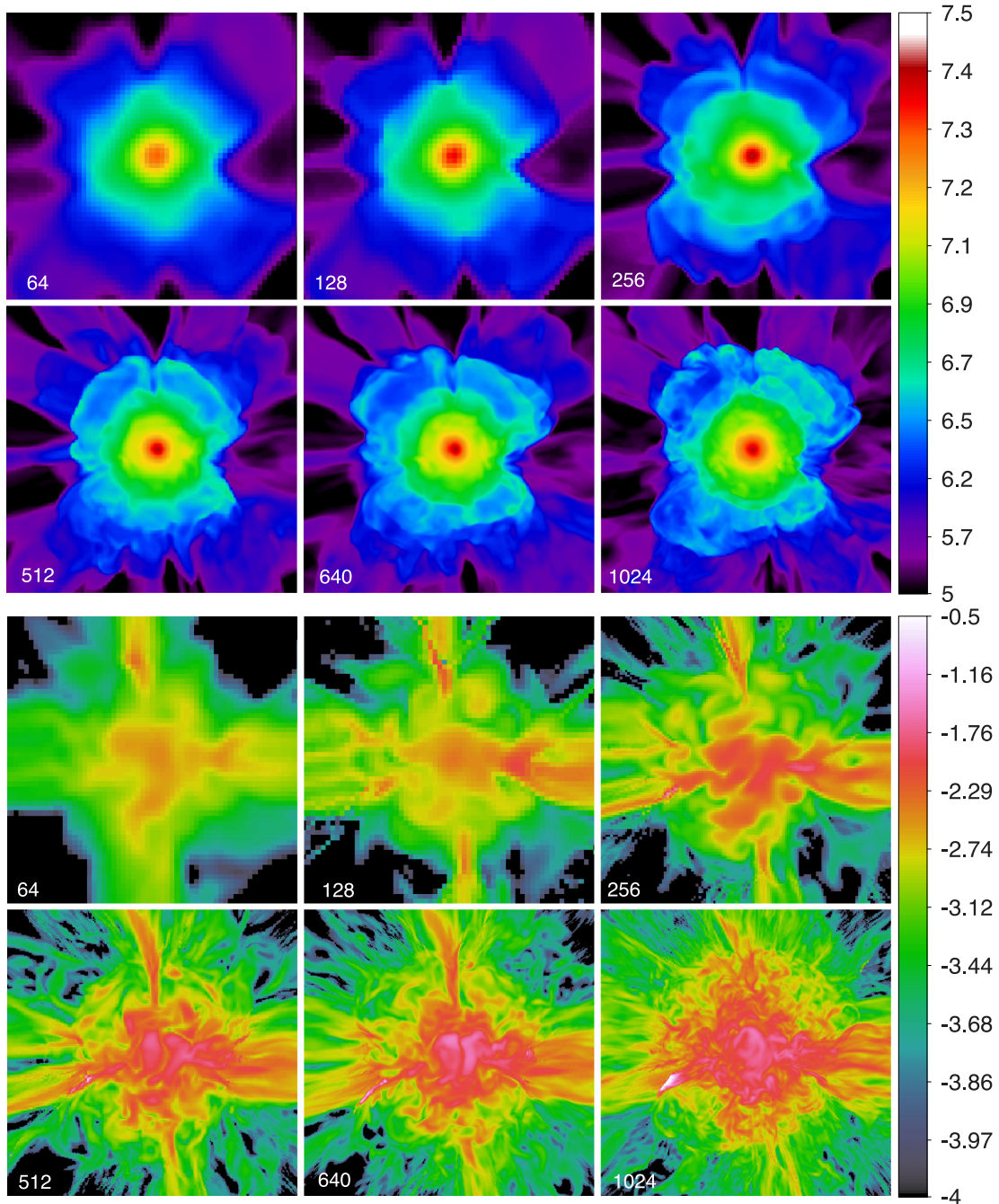


**Figure 1.** Slices through the centre of small ( $12 \text{ Mpc}^3$ ) set of fixed grid runs centred on a  $\sim 10^{14} \text{ M}_\odot$  cluster, showing the  $\log_{10}(T \text{ [K]})$  for increasing resolutions (top) and the average magnetic field strength along the line of sight ( $\log_{10} B \text{ [\mu G]}$ , bottom).

The build-up over time of the small-scale magnetic field is shown in Fig. 4 for our  $1024^3$  run.<sup>2</sup> The dependence on resolution is

<sup>2</sup>We observe that at scales close to the resolution of the box, i.e.  $k \sim 256$  in Fig. 4a spurious effect on the magnetic spectra is caused by the small-scale waves used by the Dedner cleaning to preserve  $\nabla \cdot \mathbf{B} = 0$ . We found this effect particularly in the small-scale fields in the cold hypersonic flows outside of clusters and filaments. Here, the energy equation is evolved adopting the dual energy formalism (Bryan G. L. et al. [The Enzo Collaboration], 2014), a regime where the exact conservation of hydro/MHD quantities is non-trivial due to the large unbalance between the kinetic and the internal gas energy of cells.

stronger for the magnetic field than for the velocity field, and the highest resolution run shows a final magnetic field energy which is a factor of  $\sim 10^3$  larger than that of the lowest resolution run. The small change of the final magnetic energy going from  $640^3$  to  $1024^3$  (where actually the total magnetic energy is slightly lower, an effect we ascribe to tiny variations in the non-linear evolution of the MHD structure within the volume) suggests that no further increase in the spatial resolution can produce a significant increase in the magnetic field amplification.

Fig. 5 shows the evolution of  $\int E_v(k)dk$  and  $\int E_B(k)dk$  for all runs, where we integrated the spectra only from  $k_{\text{cl}} \geq 4$  in order to focus on the kinetic/magnetic energy fluctuations contained within

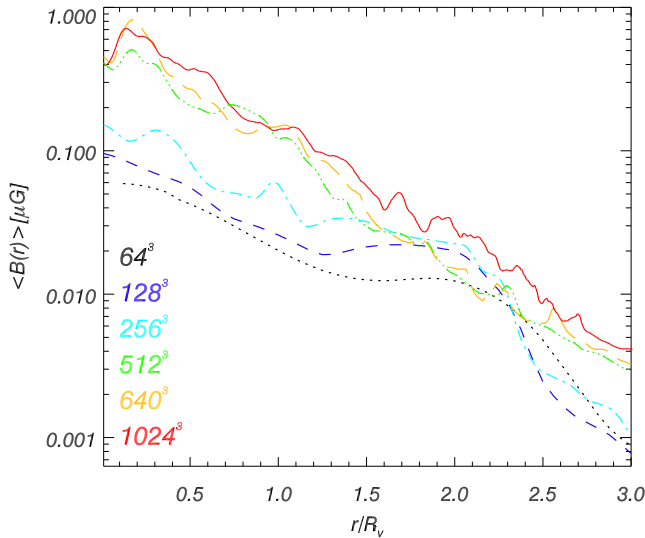


**Figure 2.** Average profile of the magnetic field at  $z = 0$  for our cluster runs at all resolutions.

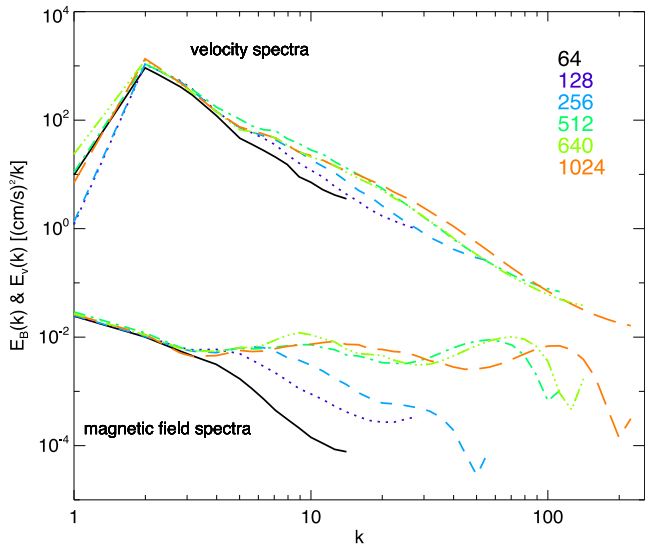


**Figure 3.** Specific kinetic energy (top lines) and magnetic (lower lines) spectra for a volume of  $(7 \text{ Mpc})^3$  centre of the cluster of Fig. 1 for all simulated resolutions. The spatial frequency,  $k$ , is in units of the box size and for each run goes from  $k = 1$  ( $7 \text{ Mpc}$ ) to the Nyquist frequency of each spectrum (i.e. twice the grid resolution of each run).

the cluster volume ( $1/k_{\text{cl}} \propto R_v$ , where  $R_v \sim 1.5 \text{ Mpc}$  at  $z = 0$ ). The total comoving kinetic energy per unit of mass is smaller by one order of magnitude going from  $z = 10$  to 0. This is an effect of the thermal dissipation of infall motions via shock heating and turbulent dissipation, and the increase of the small-scale kinetic energy as a function of resolution is only modest, i.e. a factor of  $\sim 3$  by  $z = 0$ . On the other hand, the small-scale magnetic energy is increased by a factor of  $\sim 10^6$  by the end of the run. Even in this case, the amplified field is far from equipartition with the velocity field at all scales, even if the difference at the smallest scale is small ( $E_B/E_v \sim 0.1 - 0.3$  for  $k \sim 100$ ) and in the fully saturated stage the peak of the small-scale magnetic energy is expected to drift to even smaller scales (e.g. Bhat & Subramanian 2013).

In summary, our tests confirm the start of small-scale turbulent amplification of magnetic fields at high resolution. The typi-

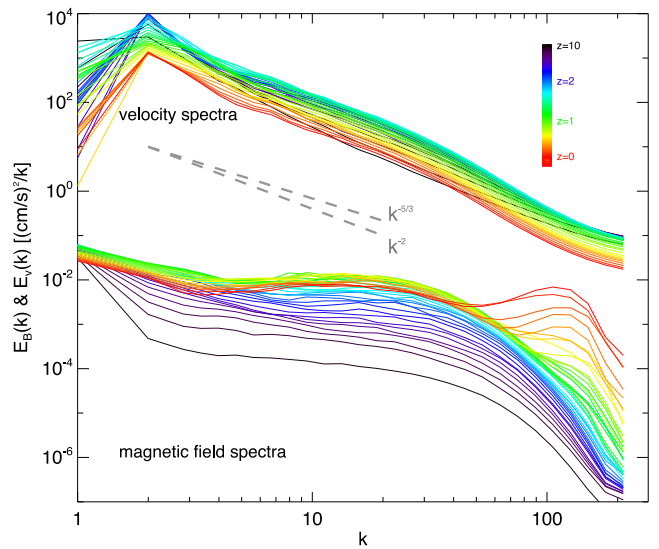


**Figure 4.** Evolution of (comoving) velocity (top lines) and magnetic (lower lines) spectra for the  $1024^3$  cluster run. The additional horizontal lines show the reference slopes of  $k^{-5/3}$  and  $k^{-2}$ .

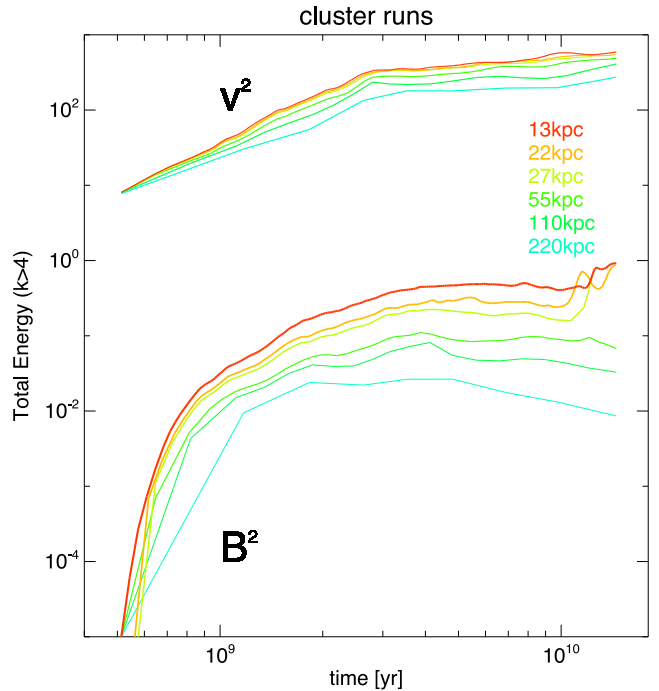


**Figure 5.** Evolution of the total kinetic energy per unit mass inside the cluster volume of Fig. 1 (top lines) and of the total magnetic energy for the same volume, as a function of resolution. The energies are given in  $[(\text{cm s}^{-1})^2]$ .

cal magnetic field strength reaches a maximum of  $\sim 0.7 \mu\text{G}$  in the cluster centre. Even if the exact level of the amplification might depend on numerical details and codes (e.g. Dolag et al. 1999; Brüggen et al. 2005; Xu et al. 2009; Bonafede et al. 2010; Collins et al. 2010), our results are in agreement with the basic scenario of turbulent amplification of primordial fields to explain the observed magnetization of galaxy clusters.

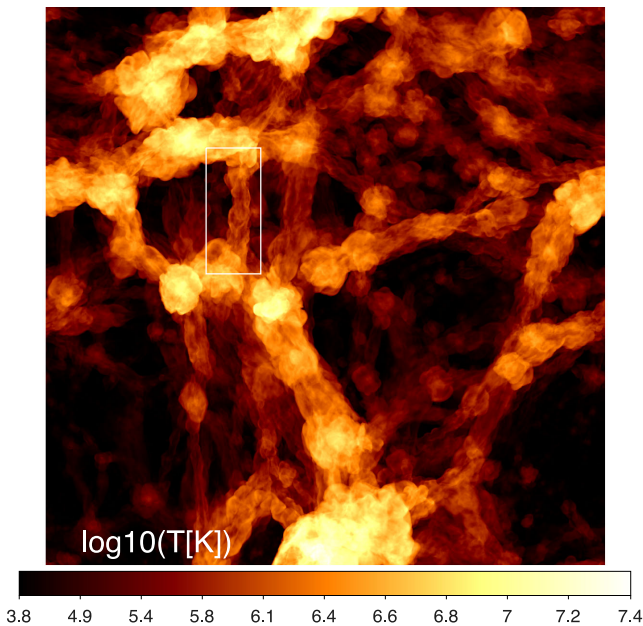


**Figure 6.** Projected (volume-weighted) temperature for the parent  $512^3$  simulation of a  $(75 \text{ Mpc})^3$  volume at  $z = 0$  that we used to re-simulate the evolution of a massive filament (within the white selection) in Section 3.2.

### 3.2 Magnetic field amplification in filaments

In a separate set of MHD runs, we investigated the amplification of the primordial magnetic field in a cosmic filament. Here, we used the canonic value of  $\sigma_8 = 0.8$  and started from a larger cosmological volume  $(75 \text{ Mpc})^3$ , in which we selected a massive  $\sim 15 \text{ Mpc}$  long filament which may be regarded as representative (as shown in the large-scale view of Fig. 6). As before, we initialized the primordial field at  $z = 30$  as a uniform field with strength  $B_0 = 10^{-10} \text{ G}$  (comoving). Fig. 7 shows the final magnetic field in a central slice through all our filament runs at  $z = 0$ . The magnetic field is the highest close to the major axis of the filament, and its maximum observed strength is only of a few  $\sim \text{nG}$ . Fig. 8 shows slices of gas temperature, velocity, and magnetic field through the centre of the filament along its length taken at different epochs. The filament is already in place at  $z = 1$  and connects two  $\sim 10^{14} \text{ M}_\odot$  clusters (that are located outside of the AMR region). Its peripheral regions feature strong ( $M \sim 10-100$ ) accretion shocks along its extension, where the accreted smooth gas (that mostly falls into it along the perpen-

dicular of the accretion region) is shock-heated to a few  $\sim 10^6 \text{ K}$ . Downstream of accretion shocks inside the filament, most of the gas flow is supersonic, as the sound speed at  $T \sim 10^6 \text{ K}$  is  $c_s \approx 100 \text{ km s}^{-1}$ , lower than the measured velocities (which are  $\sim 100-300 \text{ km s}^{-1}$ ). The magnetic field increases from  $\sim 3 \times 10^{-11} \text{ G}$  to a few  $\sim 10^{-9} \text{ G}$  downstream of the shocks. After this first boost, there is little further amplification within the filament and even the most magnetized patches hardly reach  $\sim 10^{-8} \text{ G}$ . We have highlighted some of these patches in Fig. 9, where we compared the velocity field and the magnetic field strength within a slice through the filament. Although there is no one-to-one correlation between velocity field and magnetic field, the observed trend suggests that further amplification within the filament occurs in the proximity of shocks or regions where gas flows collide. However, there is little evidence of eddies with strong curling motions. This is quite different from clusters at comparable resolution. If we rescale the number of cells by the width of the filament, our most resolved run here is comparable to our  $1024^3$  cluster run in terms of the maximum Reynolds number in the flow.

In order to test convergence, we re-simulated the same initial conditions with four different resolutions on a fixed grid (from  $64^3$  to  $512^3$  cells/DM particles). The filament we have chosen is roughly oriented along the  $z$ -axis of the grid (Fig. 6), which also enabled us to perform additional AMR runs by restricting the region for the active refinement to a narrow rectangular selection within the root grid volume. Thus, we have re-simulated the region with up to two more levels of refinement (reaching a maximum resolution of 36 kpc). By the end of its evolution, the filament reaches a transverse size up to  $\sim 4 \text{ Mpc}$ , corresponding to  $\sim 200$  cells in our AMR runs with three levels. In AMR runs, we let ENZO refine the cell size by a factor of 2 wherever the local gas density exceeded the density at the level  $l$  by factor  $\Delta = \rho_l / \rho_{l-1}$ , where we have set  $\Delta = 3$ . As previously remarked, the use of AMR may not be optimal for the study of magnetic fields since refining on matter overdensity alone can artificially suppress turbulence in regions that are relevant for dynamo amplification (e.g. Xu et al. 2009). For this reason, in a control run with one AMR level, we also enabled AMR wherever the velocity jump along any of the coordinate axes was larger than  $\Delta_v = |v_{j+1} - v_{j-1}| / |v_j|$ , as in Vazza et al. (2009). The results are very similar to those obtained adopting the density refinement criterion only, since the turbulent velocity field within the filament is mostly supersonic (Ryu et al. 2008), and the density variations within it are large enough for our conservative choice for  $\Delta$  to trigger refinements in most of its interior. It turns out that from redshift  $z = 1$ , roughly 20–25 per cent of our AMR region is covered by cells

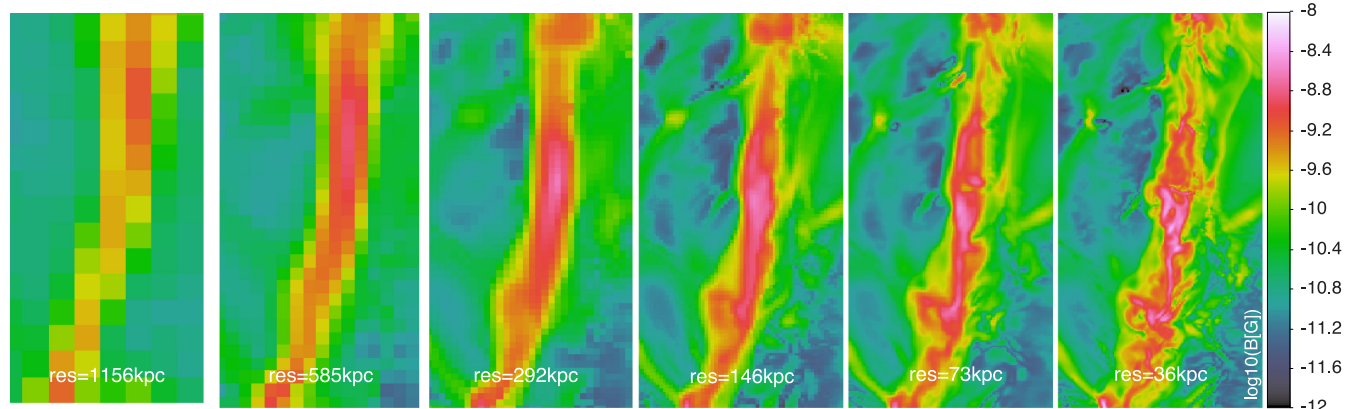


**Figure 7.** Slices of magnetic field strength in a filament with increasing spatial resolution, at  $z = 0$ . The size of each slice is  $9 \text{ Mpc} \times 18 \text{ Mpc}$ .

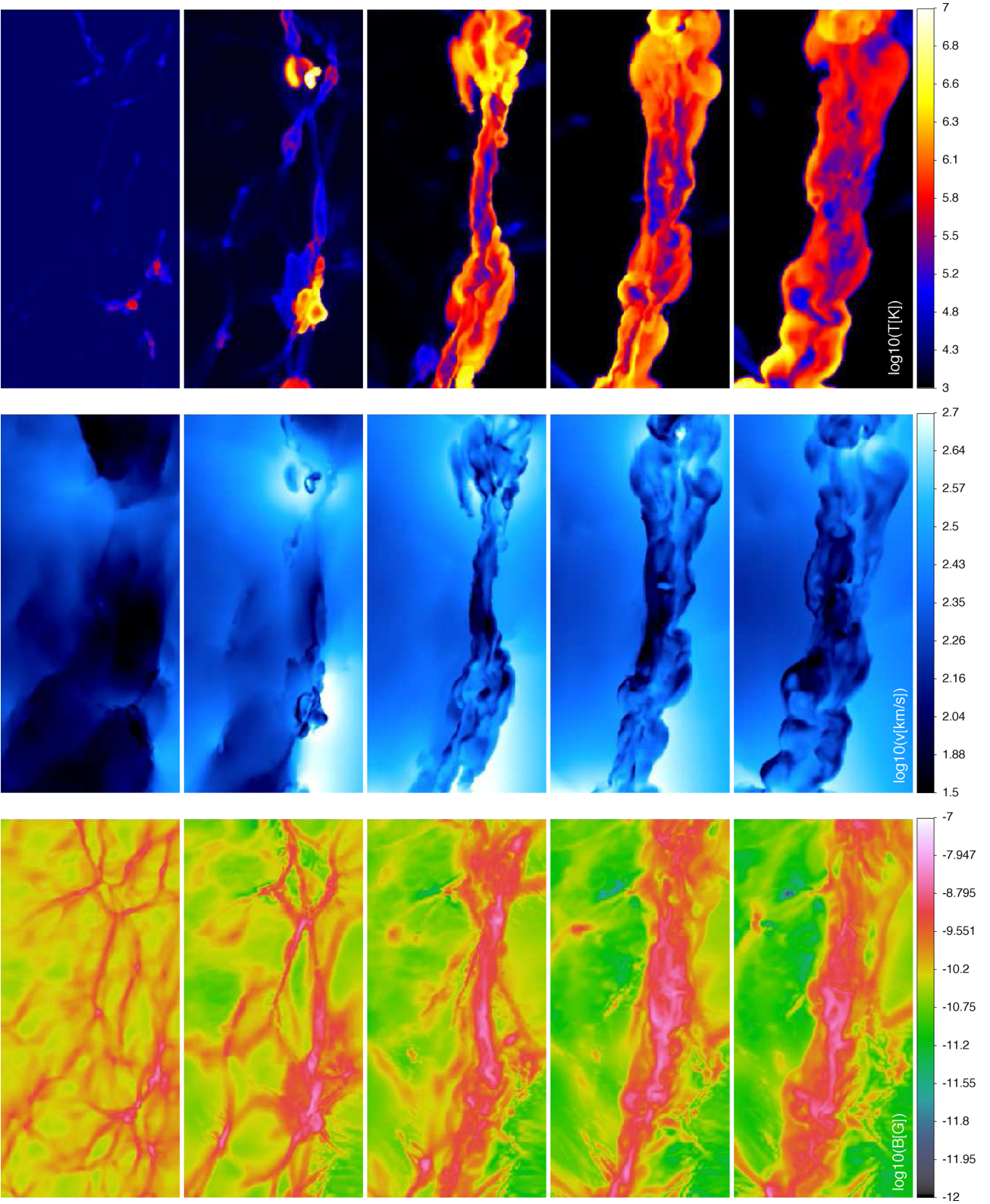


**Figure 8.** Evolution of the filament in a simulation with  $512^3$  cells and two levels of AMR (the peak resolution is 36 kpc). From top to bottom, the fields shown are: gas temperature, velocity modulus and magnetic field strength, for a thin slice of depth 36 kpc. The sides of each image measure  $9 \text{ Mpc} \times 18 \text{ Mpc}$ . From left to right, the redshifts are  $z = 4.6, 1.8, 0.9, 0.4$ , and  $z = 0$ .

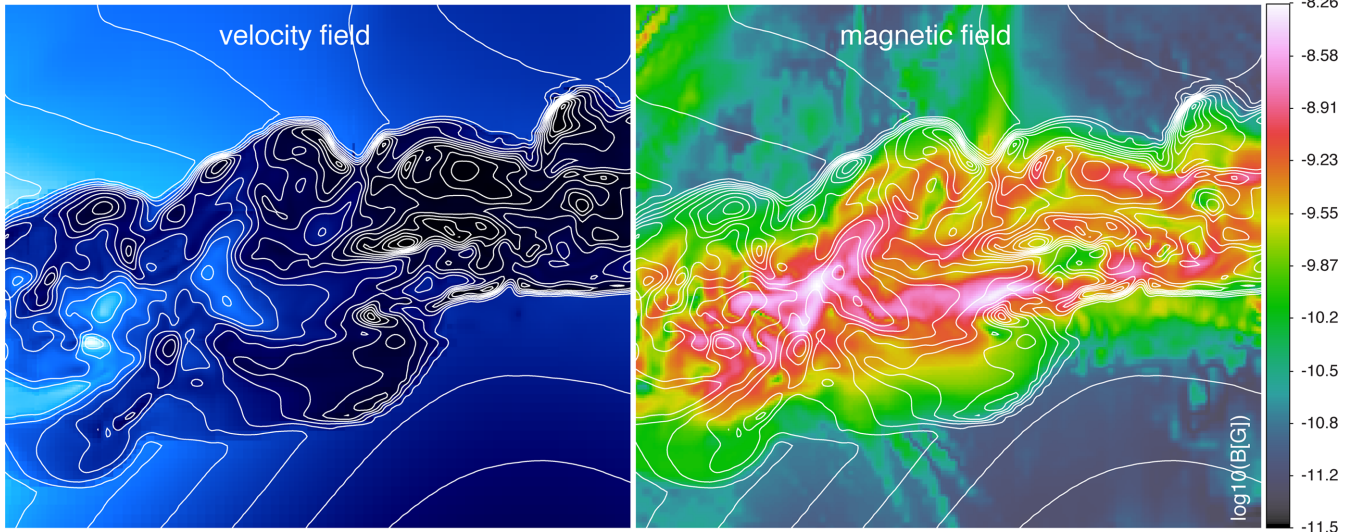


**Figure 9.** Details of the gas velocity flow (left) and of the magnetic field strength (right) for a central slice through the simulated filament of Fig. 8. The contours are the same in both panels and show the isocontours of the velocity field. The size of the image is  $9 \text{ Mpc} \times 7 \text{ Mpc}$  and the peak resolution is 36 kpc.

**Table 2.** Main parameters of our MHD runs of a cosmic filament, referred to in Section 3.2. Column 1: number of grid(s) cells in the initial conditions; column 2: spatial resolution; column 3: dark matter mass resolution; column 4: AMR levels (D = refinement based on the local gas overdensity; V = refinement based on the local velocity jump).

| $N_{\text{grid}}$ | $\Delta x$ (kpc) | $m_{\text{DM}}$ ( $M_{\odot} h^{-1}$ ) | AMR |
|-------------------|------------------|--|-----|
| $64^3$            | 1170             | $1.22 \times 10^{11}$                  | 0   |
| $128^3$           | 585              | $1.52 \times 10^{10}$                  | 0   |
| $256^3$           | 292              | $1.90 \times 10^9$                     | 0   |
| $512^3$           | 146              | $2.38 \times 10^8$                     | 0   |
| $512^3$           | 73               | $2.38 \times 10^8$                     | 1D  |
| $512^3$           | 73               | $2.38 \times 10^8$                     | 1DV |
| $512^3$           | 36               | $2.38 \times 10^8$                     | 2D  |

at the highest resolution ( $\approx 6.55 \times 10^6$  cells), corresponding to more than an  $\sim 60$ –70 per cent of the volume occupied by the filament within the AMR region itself. Incidentally, the same choice would not work for galaxy clusters, where the density varies more gently and the turbulence is subsonic (Xu et al. 2009; Vazza et al. 2009). The parameters for this set of simulations are summarized in Table 2.

The velocity spectra for our run with the highest resolution display a similar evolution as in the cluster (Fig. 10), and present a well-defined power law (compatible with  $\propto k^{-2}$ ) for nearly two decades in scale. The magnetic spectra again do not show a clear power-law behaviour, and show small-scale bumps which evolve with time. However, the build-up of the small-scale magnetic structure is much less significant than in the ICM. Moreover, the trend does not increase over time but reaches its maximum around  $z \sim 1$  (green lines), while the small-scale power is  $\sim 1$ –2 orders of magnitude smaller at  $z = 0$ . Overall, the magnetic spectra seem to evolve much faster towards their maximum, compared to the case of the ICM, but since  $z \sim 1$  they do not show significant evolution on most scales. The maximum in the magnetic field spectra on small scales ( $k \geq 80$ , corresponding to  $\leq 200$  kpc) is matched by an excess of velocity power at the same scales. The time corresponds to the epoch in which the filamentary region that connects the two forming clusters assembles most of its mass, and when shock heating

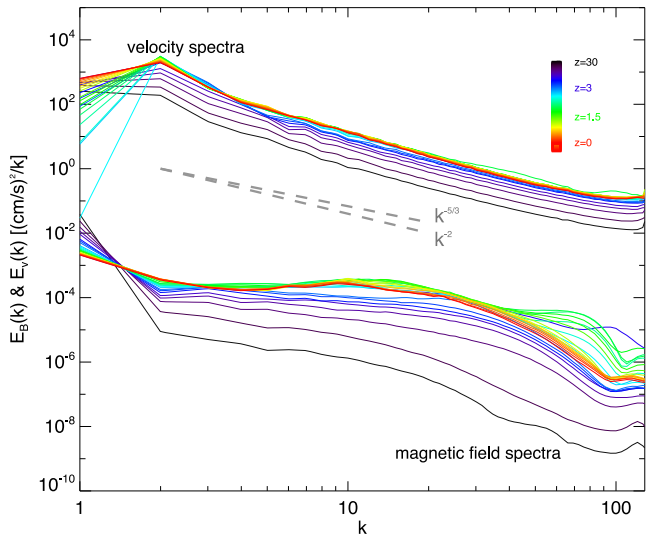


**Figure 10.** Evolution of the comoving velocity spectra (top lines) and of the comoving magnetic spectra (lower lines) for our filament run with  $512^3$  cells and two AMR levels. The additional horizontal lines show the reference slopes of  $k^{-5/3}$  and  $k^{-2}$ . The spatial frequency,  $k$ , is in unit of the box size and for each run goes from  $k = 1$  (18 Mpc) to the Nyquist frequency of each spectrum (i.e. twice the grid resolution of each run).

raises the warm-hot-intergalactic medium (WHIM) temperature to  $\geq 10^6$  K (Fig. 8). At this time, gas flows into the filament from opposite sides at large velocities, and compresses the magnetic fields. Still, the plasma beta is only of the order of  $\beta \sim 10^5$ – $10^6$  in the filament.

The dependence on resolution of the power spectra (Fig. 11) is similar to that of clusters (Fig. 3), and runs with higher resolution show the build-up of small-scale magnetic fields, even if less evident than in the ICM. For comparison, at  $k = 10$  the magnetic power spectra increases by more than a factor of  $\sim 100$  in the ICM run when the resolution is increased by a factor of 8, while this is less than a factor of  $\sim 10$  in the filament.

The integrated velocity and magnetic spectra as a function of time are given in Fig. 12. Again, we filtered out scales smaller than

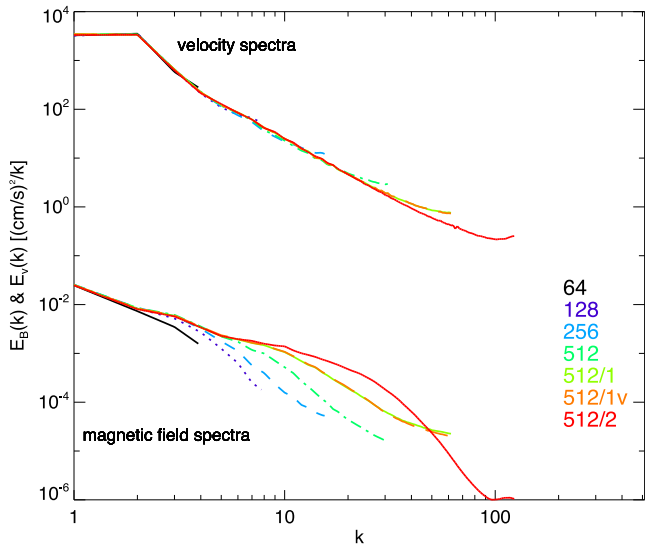


**Figure 11.** Comparison of the velocity spectra (top lines) and of the magnetic spectra (lower lines) for our filament runs (Section 3.2) at  $z = 0$  for different resolutions. The units of the spatial frequency  $k$  are as in Fig. 10.

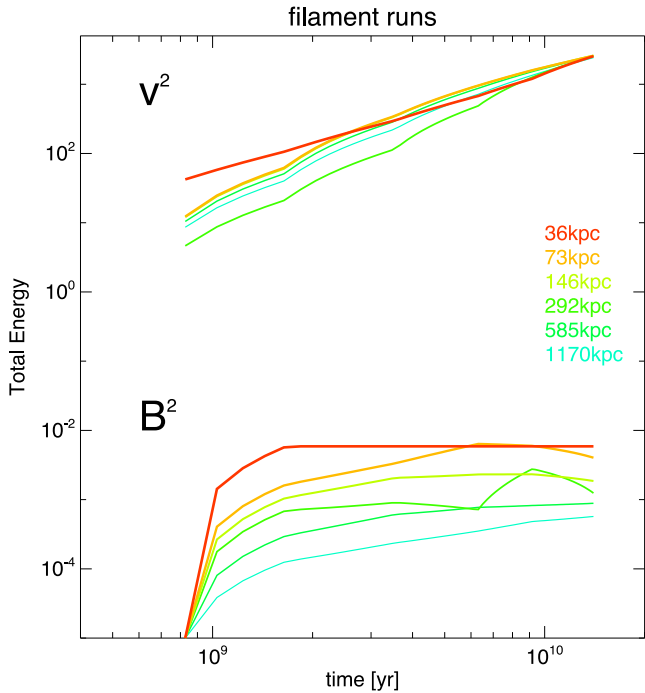


**Figure 12.** Evolution of the total kinetic energy per unit of mass inside the filament volume (top lines) and of the total magnetic energy for the same volume, as a function of resolution. The energies are given in  $(\text{cm s}^{-1})^2$ .

the mean diameter of the filament at  $z = 0$ , to focus only on velocity and magnetic field fluctuations that are roughly contained within the filament ( $\leq 4$  Mpc). The continuous accretion of matter on to the filament causes the growth of both quantities: during the whole evolution the specific kinetic energy has increased by  $\sim 2$  orders of magnitude, while the magnetic energy has increased by  $\sim 3$  orders of magnitude in our best resolved runs, and  $\sim 2$  orders of magnitude in our coarsest run. This is very different from our previous results for clusters (Fig. 5). While the increase of specific kinetic energy is similar, the increase of magnetic energy with resolution is much

slower with resolution, indicating that convergence might be within reach. This suggests that starting from a resolution of the order of 73 kpc ( $\sim 1/60$  of the thickness of the filament) or better, the effects of compressive modes and shocks on the final magnetic field does not increase with resolution.

We conclude that despite the large dynamical range of scales of our AMR runs (corresponding to a Reynolds number of  $\sim 210$  in our most resolved case, by assuming that the outer scale is the average diameter of the filament,  $\sim 4$  Mpc), in our simulated filament we do not observe a significant small-scale dynamo. Moreover, the trend with resolution of spectra and integrated quantities indicates that the lack of efficient amplification is robust against further increase in resolution, thereby limiting the maximum amplification factor to  $\sim 100$  for the magnetic energy in the WHIM for this object. In Section 4, we will discuss this further.

### 3.3 Larger cosmological runs

Given the limited statistical significance of results obtained with single objects, we proceed to large-scale unigrid cosmological simulations comprising hundreds of clusters and filaments. As before, we initialized the magnetic field with a uniform  $B_0 = 10^{10}$  G at  $z = 30$  and employed the Dedner scheme on the MHD version of ENZO (Wang et al. 2010).

First we present our largest run: a  $(50 \text{ Mpc})^3$  volume simulated with  $2400^3$  cells and DM particles (resolution 20.8 kpc), which, as far as we know, is the largest MHD cosmological simulation to date. The simulation used  $\sim 4.5$  million core hours running on 512 nodes (2048 cores in total) on Piz Daint. The resolution was chosen such that at least a cell size of  $\sim 20$  kpc could be achieved in order to obtain sufficient amplification in  $10^{14} \text{ M}_\odot$  haloes. The simulation box is large enough in order to contain massive galaxy clusters with a concordance model  $\sigma_8$ .

Fig. 13 shows the projected (mass-weighted) magnetic field strength at  $z = 0$  across the whole volume. In regions of large overdensities, the magnetic field is amplified beyond the effect of compression by twisting motions driven by accretion and mergers. Twisted magnetic field structures are found only close to the centre of haloes or in the proximity of the main axis of filaments. The maximum field attained in filaments hardly reaches  $\sim 10$  nG, while in the most massive haloes the maximum magnetic field is of the order of  $\sim 0.05$ – $0.1$   $\mu$ G at most.

The average  $B(n)$  (Fig. 14) shows that, for the largest part, the magnetic field scales as  $B \propto n^{2/3}$  with little scatter. At high densities, the large number of small haloes dominates the average and cause a flattening of the relation because of the small number of massive hot clusters.<sup>3</sup> For this reason, we also plot (red lines) the average relation obtained only using cells with  $T \geq 10^7$  K, which highlights the ICM. Then the upper envelope of the average reaches  $\sim 0.1$   $\mu$ G at densities typical of cluster centres, which is an effect of the small-scale dynamo (Section 3.1). However, for the concordance value of  $\sigma_8 = 0.8$  the high-mass clusters form late in time compared to the cluster previously simulated and hence the amplification by  $z = 0$  is less efficient by the end of the run. The rather small final mass/size of the clusters formed in the  $(50 \text{ Mpc})^3$  is too small to

<sup>3</sup>A flat relation,  $B(n)$ , at high densities has also been reported by Skillman et al. (2013) using ENZO MHD simulations with Constrained Transport (Collins et al. 2010). A possible explanation for the level of flattening measured in their and our runs is an excess of numerical magnetic reconnection due to finite spatial resolution.

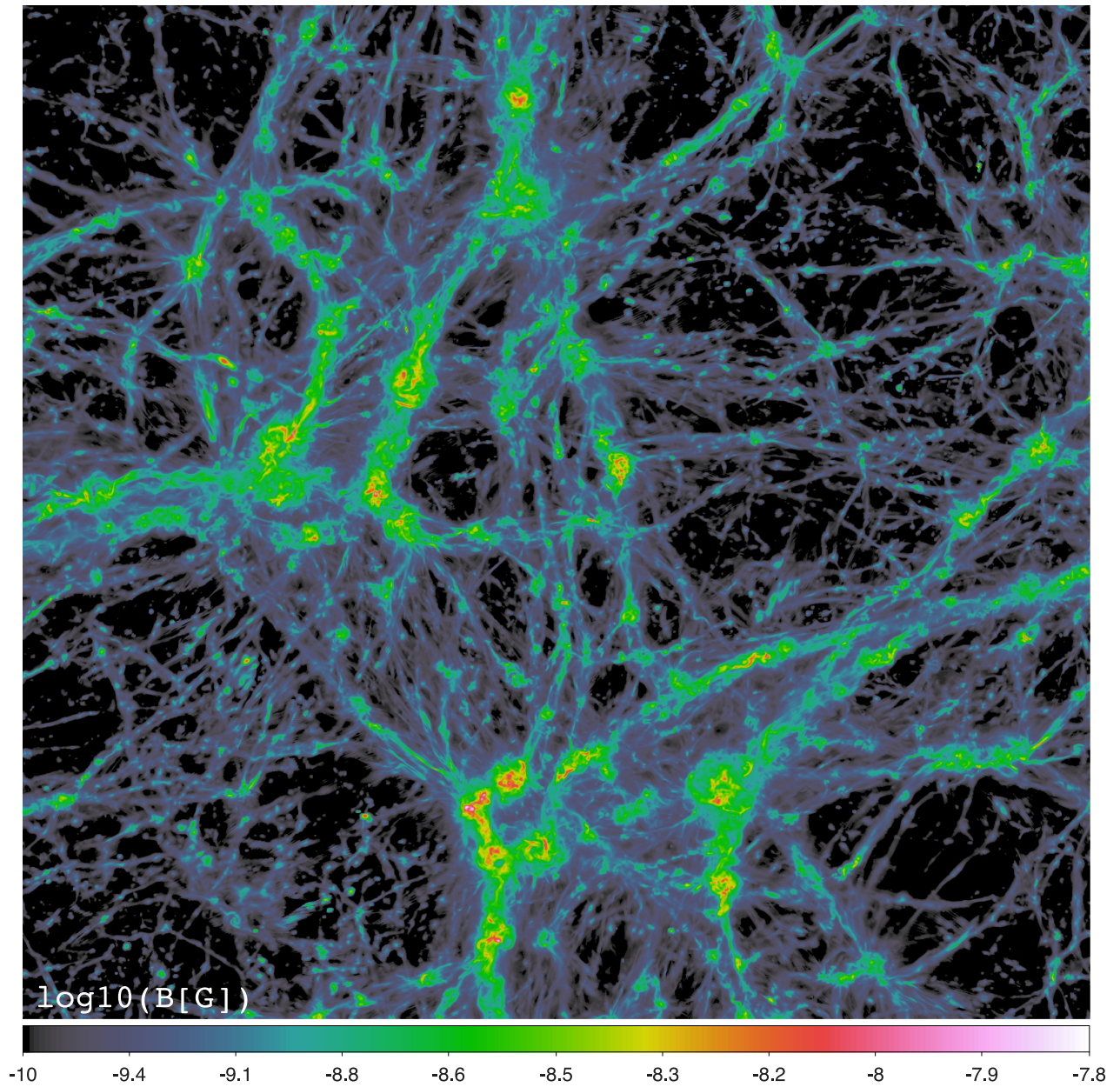


Figure 13. Projected (density weighted) magnetic field intensity for our  $2400^3$  simulation of a  $(50 \text{ Mpc})^3$  volume at  $z = 0$ .

probe large Reynolds numbers for most of the simulated objects. Our high-temperature threshold selects objects with virial masses above  $\sim 5 \times 10^{13}$ – $10^{14} M_\odot$ , i.e. with virial radii around  $\sim 1 \text{ Mpc}$ . In this case the virial radius is sampled with at least  $\geq 150^3$  cells at  $z = 0$ , and the numerical Reynolds number of the flow is  $R_e \sim 500$  (equation 1). This fulfils the criterion proposed by Federrath et al. (2011b) and Latif et al. (2013), according to which a minimum amount of  $128^3$  cells per Jeans length is necessary to obtain dynamo effects in primordial haloes. At the overdensity typical of filaments,  $n/\langle n \rangle \sim 1$ – $10$ , the average magnetic field is  $\leq 10 \text{ nG}$ , as found in our previous filament runs.

### 3.4 Additional magnetic field seeding by galaxies

Finally, we investigate the possible role of additional magnetic field seeding from galaxies crossing the filament. In a simulation

box of  $(25 \text{ Mpc})^3$  sampled by a  $1200^3$  mesh, we tested the effect of releasing additional magnetic fields as small magnetic loops injected at the estimated location of forming galaxies. The location of each presumed galaxy was assigned based on a (comoving) gas overdensity larger than 500 times the critical gas density, and at the centre of each overdense region we injected a magnetic loop ( $3^2$  cells across) with a total magnetic field strength corresponding to  $\beta = 100$  at the location of each galaxy. For the sake of simplicity, we enabled the seeding from galaxies only once at  $z = 2$ , and compared the results at  $z = 0$  to the model with purely primordial seeding. This model can only test the efficiency of magnetization of filaments and galaxy clusters through stripping and mixing of gas from magnetized haloes in the course of their motions inside large-scale structures. Note that our seeding model does not include the additional effect of gas outflows driven by winds and AGN.

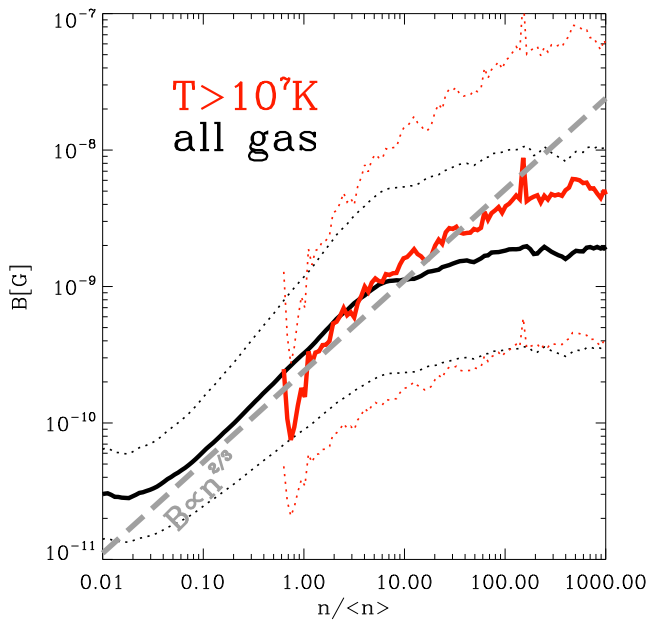


**Figure 14.** Average relation between magnetic field and gas density for  $(50 \text{ Mpc})^3$  with  $2400^3$  cells at  $z = 0$ . The black lines show the magnetic-energy weighted average  $B$  for all cells as a function of density (solid = mean, dotted =  $\pm 3\sigma$  scatter), while the red lines show the relation computed only for  $T \geq 10^7 \text{ K}$  cells to better mark the trend in galaxy clusters. The additional grey line shows the expected trend for pure compression ( $B \propto n^{2/3}$ ).

The additional seeding magnetizes the high-density ICM leading to field strengths of up to of  $\sim 0.1\text{--}1 \mu\text{G}$  at the centre of the most massive haloes at  $z = 0$ . The distribution function of magnetic energy and the average  $B(n)$  (Fig. 15) shows how the galactic seeding has the greatest effect in haloes ( $n/\langle n \rangle \geq 100$ ). There, the final magnetic field is  $\sim 10\text{--}30$  times larger, reaching  $\sim 0.3 \mu\text{G}$  even in the low-mass haloes formed in this smaller box. However, the effect outside of these haloes is quite limited since only the  $B \geq 10 \text{ nG}$  is significantly affected by the additional seeding from galaxies (bottom panel).

In summary, while more complex time-dependent model of magnetic seeding from high-redshift galaxies are required, our results do not show significant large-scale magnetization by the simple advection and stripping of magnetized galaxies. The inclusion of fast (or continuous) magnetized outflows driven by galactic activity might yield different results. SPH simulations by Donnert et al. (2009) have shown that the magnetization of the cosmic web outside of haloes in galactic seeding scenarios is very model dependent.

## 4 DISCUSSION

We have investigated the amplification of primordial magnetic fields as a function of spatial resolution. Our results can be summarized as follows.

(i) *Magnetic field amplification in the ICM*: we have simulated the small-scale dynamo in a galaxy cluster with uniform grids of increasing resolution (from 220 to 13 kpc). At resolutions with cell sizes below  $\sim 26 \text{ kpc}$ , we observe the emergence of small-scale power in the magnetic energy spectra. The amplification seems to have reached convergence at the maximum resolution of 13 kpc (i.e.  $\sim 1/100$  of the cluster virial radius at  $z = 0$ ), at least inside the virial region. The magnetic fields reach  $\sim 0.4 \mu\text{G}$  in the cluster core, corresponding to  $\sim 1/100$  of the thermal energy of the cluster

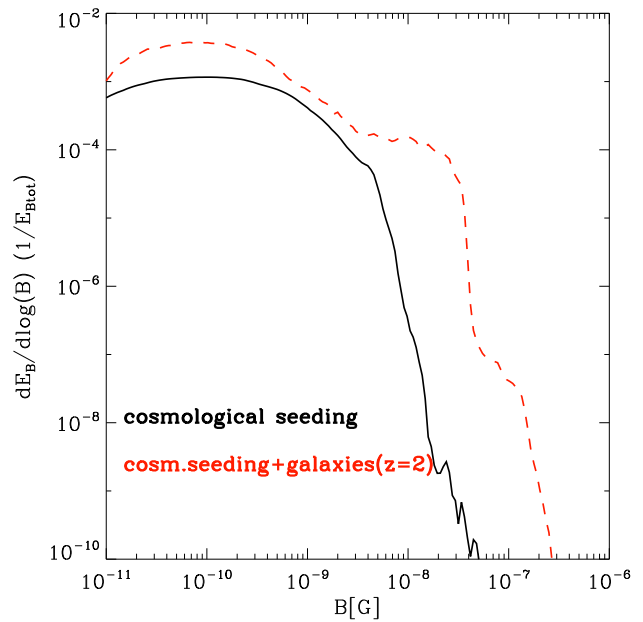
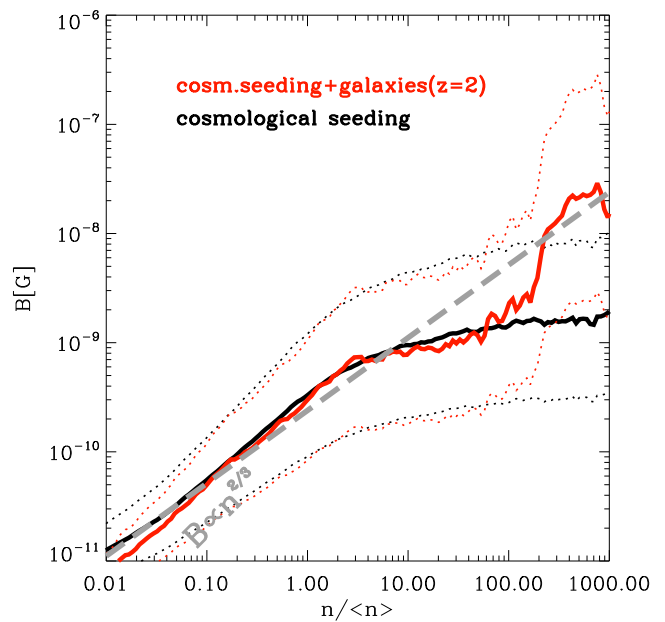


**Figure 15.** Top panel: average relation between magnetic field and gas density (as in Fig. 14) for two resimulations of  $(25 \text{ Mpc})^3$  volume at  $z = 0$ , with a cosmological weak magnetic field initialized at  $z = 30$  (black) or with the additional release of magnetic loops from ‘galaxies’ in the volume at  $z = 2$  (red). The additional grey line shows the expected results for pure compression. Bottom panel: energy-weighted distribution of magnetic fields for the same runs.

within the same volume. Although our setup is rather artificial (due to the use of an artificially large value of  $\sigma_8$  in order to enable the growth of a massive cluster inside a small cosmic volume), the results are in agreement with previous results (Dolag et al. 1999; Brüggen et al. 2005; Dubois & Teyssier 2008; Donnert et al. 2009; Collins et al. 2010).

(ii) *Magnetic field amplification in cosmic filaments*: in filaments, the maximum amplification factor for the magnetic energy is of the order of  $\sim 100$  and the maximum field strength, close to the axis of the filament, hardly reaches  $\sim 0.01 \mu\text{G}$ . The corresponding magnetic

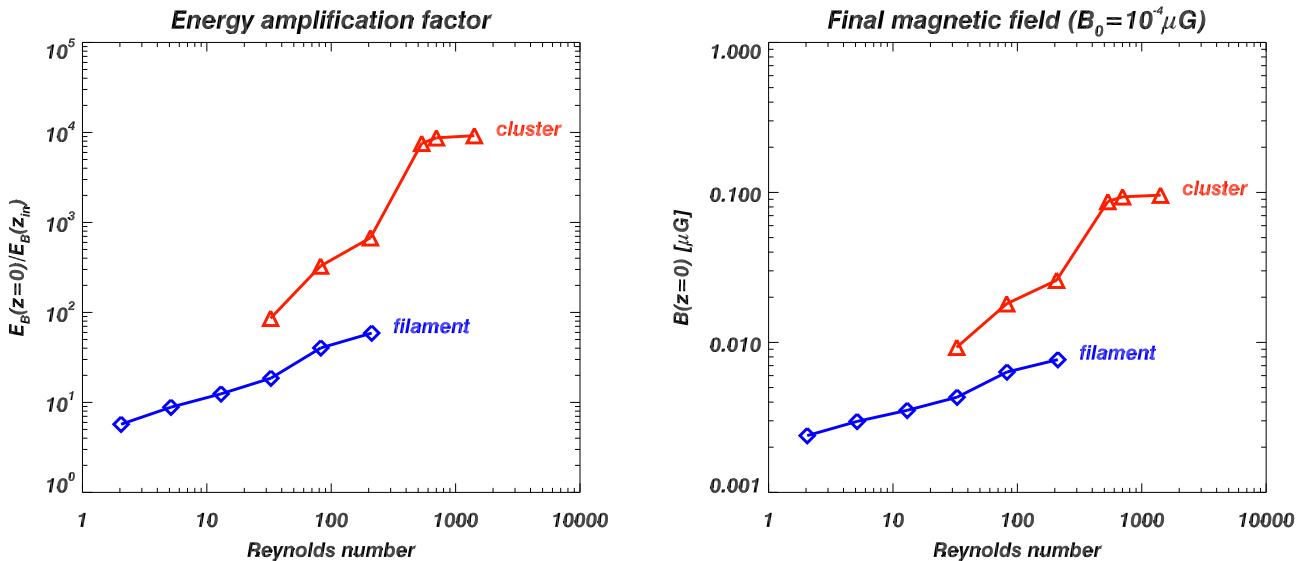


**Figure 16.** Amplification of magnetic energy as a function of numerical resolution (top) and Reynolds numbers (centre), for the clusters and filaments. Bottom panel: average magnetic field at  $z = 0$ , considering a uniform seed field of  $B = 10^{-10}$  G. The Reynolds numbers of each run is computed as in equation (1), based on the typical size of the cluster ( $\sim 3$  Mpc) and of the filament ( $\sim 4$  Mpc).

energy is only  $\sim 10^{-5}$  of the gas kinetic energy, smaller than what is found in driven turbulence simulations (e.g. Federrath et al. 2011a). The physical reason for this is discussed in the next Section.

These results seem to be independent of resolution and apply up to the largest Reynolds number we could probe here,  $R_e \approx 200$ . The independence of resolution stems from the fact that the ratio of kinetic energy of compressive and solenoidal modes within the filament does not change significantly with resolution. Compressive forcing only leads to inefficient magnetic field amplification.

(iii) *Amplification as a function of environment:* inside haloes where the virial volume is sampled with enough resolution elements ( $\geq 150^3$  inside the virial volume) we find some dynamo amplification, as suggested by Federrath et al. (2011b) and Latif et al. (2013). The additional release of stronger magnetic fields from the high-density peaks of haloes (here assumed to take place only once at  $z = 2$ ) does not affect the magnetic fields in filaments at  $z = 0$ . However, it does increase the magnetization of the ICM at  $z = 0$ , due to stripping and further mixing of the additional magnetic field in the turbulent ICM.

#### 4.1 What is the difference between the small-scale dynamo in clusters and filaments?

Fig. 16 summarizes our results for the amplification of magnetic field in the ICM and in the WHIM, as measured in our cluster and filament runs. The plots show the amplification of magnetic energy and of the mean magnetic field strength (averaged inside the cluster and filament volume) at  $z = 0$ , where we assigned a fiducial maximum Reynolds number to both systems from equation (1). The Reynolds numbers in the filament are smaller but the observed dependence on resolution suggest that there would be no efficient dynamo, even for fairly large numerical Reynolds numbers ( $\sim 200$ ). The magnetic fields in the ICM can be understood from simulations (Schekochihin et al. 2004; Cho et al. 2009; Jones et al. 2011) with  $P_m = 1$  (where  $P_m = \eta/\nu$  is the Prandtl number, and  $\eta, \nu$  are the magnetic resistivity and physical viscosity, respectively). They concluded that for a large enough Reynolds number an exponential growth of the field is observed, followed by a linear growth on the

time-scales of several tens of dynamical times. During the exponential phase  $B(t) = B_0 \exp(\Gamma t/\tau)$ , where  $B_0$  is the initial field strength,  $t$  is the time and  $\tau$  is a characteristic time of the system (which can be here approximated as the sound crossing time). A fast dynamo occurs only when  $\Gamma \gg 1$ . In a  $P_m = 1$  regime the relation between  $\Gamma$  and the Reynolds number is  $\Gamma \approx \frac{R_e^{1/2}}{X}$  ( $X$  is a numerical factor of the order of  $X \sim 15\text{--}30$ , from which it follows that  $R_e \geq 15^2\text{--}30^2$  to enter the exponential phase). These results suggests that even if the system is subject to continuous turbulent forcing at the largest scales, it takes several tens of crossing time for the system to reach a stationary magnetic field strength of the order of  $\sim 30$  per cent of the total kinetic energy. This is not far from what we observe, at least on the smallest spatial scales, in our simulated cluster at the highest resolution, owing to the fairly large  $R_e \sim 1400$  there. This is not observed in the filament, even at our highest resolution, with no sign of dynamo action.

Besides the smaller numerical Reynolds number in the filaments, there are additional reasons to believe that the amplification cannot be significantly larger than this – even in case of a much larger  $R_e$ . First, previous simulations by independent groups have shown that compressive forcing of turbulence is very inefficient in producing dynamo amplification, as most of the energy pumped into the system is quickly dissipated into shocks (Haugen & Brandenburg 2006; Federrath et al. 2011a; Jones et al. 2011, see also our Appendix). In particular, Federrath et al. (2011a) have shown that the magnetic field dynamo driven by forced turbulence in a box exhibits a characteristic drop of the growth rate at the transition from subsonic to supersonic turbulent flow. Solenoidal turbulence drives more efficient dynamos, due to the higher level of vorticity generation and the stronger tangling of the magnetic field. Based on the different approach of solving the Kazantsev equation with the WKB (Wentzel, Kramers, and Brillouin) approximation, Schober et al. (2012) measured the growth rate of magnetic field dynamo in different turbulent models. They showed that for highly compressible turbulence the critical Reynolds number to produce an efficient dynamo is larger than in the case of Kolmogorov turbulence (i.e.  $\sim 2700$  versus  $\sim 100$ ), and that the growth rate in the compressible case has a shallower dependence on the Reynolds

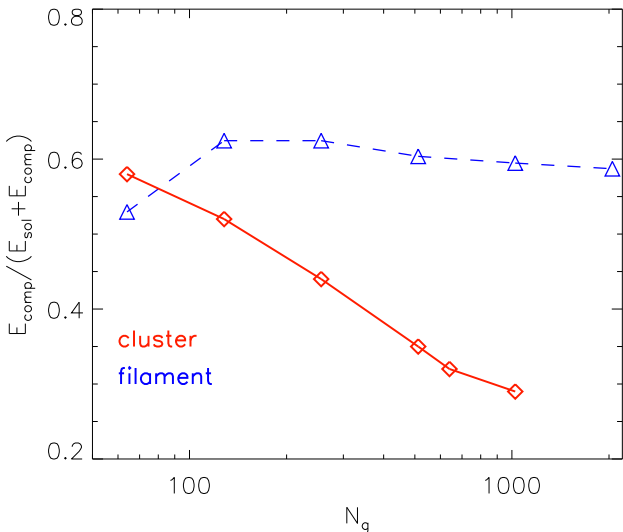


**Figure 17.** Resolution-dependence of the ratio between compressive and total (compressive+solenoidal) kinetic energy in clusters and filaments.

number (i.e.  $\Gamma \propto R_e^{1/3}$  for Burgers turbulence and  $\propto R_e^{1/2}$  for Kolmogorov turbulence). Finally, using a Fokker–Planck approach to compute the growth of magnetic field dynamo in the non-linear regime, Schleicher et al. (2013) have recently shown that the characteristic length-scale of the magnetic field grows faster in Burgers than in Kolmogorov turbulence. This confirms that in the presence of compressive forcing dynamo amplification is much less efficient than in the solenoidal forcing case. This is even more apparent in filaments because strong advection motions along the spine of filaments continuously move turbulent eddies away from the region of colliding flows, reducing small-scale dynamo more severely than in the case of stationary forcing of solenoidal turbulence in the box (e.g. Federrath et al. 2011a). Here, we have analysed how the modes of the velocity field evolve with spatial resolution in both cases. To this end, we decomposed in the velocity field using the Hodge–Helmholtz projection in Fourier space (e.g. Kritsuk et al. 2011), and computed the kinetic energy in the compressive and in the solenoidal modes. In both cases, we selected a region at  $z = 0$ , not affected by infall motions outside of accretion shocks.

The panels in Fig. 17 show our results: while in the ICM the budget of kinetic energy in compressive modes decreases with resolution, in the WHIM the energy does not change. At the best resolution, the energy in compressive modes is only  $\sim 30$  per cent in the ICM and up to  $\sim 60$  per cent in the WHIM. The fact that the kinetic energy in solenoidal motions is higher in galaxy clusters and smaller in the WHIM has already been established by cosmological numerical simulations (Ryu et al. 2008; Iapichino et al. 2011; Zhu et al. 2013; Miniati 2014). However, we find that this persists at high resolution and that in filaments  $\sim 2/3$  of the kinetic energy is in form of supersonic compressive modes. This explains the lack of amplification in filaments, despite the increase in the numerical Reynolds number. Indeed, the maximum amplification of magnetic energy in subsonic solenoidal turbulence (as in the ICM) is expected to be  $\sim 1$ – $2$  orders of magnitude higher than the maximum amplification reached in supersonic compressive turbulence (as in the WHIM) (Federrath et al. 2011a). Moreover, the growth rate in the first case is  $\sim 5$ – $10$  times faster.

#### 4.2 Physical and numerical limitations of the MHD picture

Our resolution tests went down to a resolution of  $\sim 20$  kpc even though the smallest collisional scales in the WHIM should be  $\sim 100$ – $10^3$  kpc based on pure Coulomb interactions. Below this scale a kinetic modelling could be more appropriate (Weinberg 2014). However, if efficient scattering occurs between particles and magnetic perturbations induced by small-scale plasma instabilities, then the mean free path of particles decreases in a self-regulating process: if turbulence is stronger at the scale of injection, the mean free path of plasma particles is reduced and the range of scales over which the fluid behaves as collisional is increased (Schekochihin et al. 2005; Brunetti & Lazarian 2011; Kunz et al. 2011). Whether or not the same picture applies to the even more tenuous and weakly magnetized WHIM in filaments, is presently uncertain.

Regarding the MHD scheme, the Dedner hyperbolic cleaning scheme (Dedner et al. 2002) is a robust and widely used method in the literature, but is prone to small-scale artefacts and artificial dissipation due to the  $\nabla \cdot \vec{v}$  wave necessary to limit to the presence of magnetic monopoles. In the literature, this method has been compared to others, both for grid and SPH simulations (Dedner et al. 2002; Wang & Abel 2009; Mignone, Tzeferacos & Bodo 2010; Kritsuk et al. 2011; Stasyszyn, Dolag & Beck 2013; Pakmor et al. 2014), reporting good consistency. In particular, Kritsuk et al. (2011) have investigated in detail the performance of several MHD methods in the case of decaying supersonic turbulence in an isothermal box, including the Dedner scheme implemented in ENZO. They concluded that all codes agreed well on the kinetic and magnetic energy decay rate, but they varied on the amplitude of the peak magnetic energy, as this was significantly dependent on the numerical dissipation of each method (that in turns determines the effective magnetic Reynolds number). They found that the use of explicit divergence cleaning reduces the magnetic spectral bandwidth relative to codes that preserve the condition on the magnetic field exactly, as the constrained transport (CT) methods. They concluded that codes that fall short in some of the investigated diagnostics (i.e. dissipation of small-scale modes in the Dedner cleaning scheme) still can get to the correct physical answer, provided that they compensate the higher numerical dissipation with higher numerical resolution.

#### 4.3 Comparison to previous work

Our results for non-radiative runs seem to be in agreement with those obtained by Brüggen et al. (2005), Dubois & Teyssier (2008) and Collins et al. (2010), who also reported evidence of growth of magnetic fields in excess of simple compression even if with lower efficiencies.<sup>4</sup> Runs with radiative cooling readily obtain magnetic fields of the order of  $\sim \mu\text{G}$  in the ICM, mainly as a result of overcooling (Dubois & Teyssier 2008; Collins et al. 2010; Ruszkowski et al. 2011). Despite some similarity in the magnetic spectra, it is difficult to relate to the ENZO-MHD simulations by (Xu et al. 2009, 2011) since their seeding is very different from ours.

There is disagreement, though, with the results of cosmological SPH simulations (Dolag et al. 1999; Gazzola et al. 2007; Dolag, Bykov & Diaferio 2008; Donnert et al. 2009; Dolag &

<sup>4</sup> Also the latest very high-resolution cluster simulations by F. Miniati (see Miniati 2014, for a study of the hydrodynamical properties of these simulations) confirms the difficulty to get to very large amplification factors, despite the fairly large numerical Reynolds number achieved there (private communication).

Stasyszyn 2009; Bonafede et al. 2011; Beck et al. 2012, 2013; Stasyszyn et al. 2013), that typically reach much larger amplification factors for the magnetic energy, already at high redshift ( $z \geq 2$ ). Understanding these differences is beyond the goal of this paper, and we can only speculate that the reason lies in the capability of SPH in refining the innermost regions of haloes already at earlier times. However, also the difficulty in correctly modelling small-scale velocity structures (and the connected magnetic-field amplification) in SPH might be responsible for the difference (Bauer & Springel 2012; Price 2012), for which ad hoc solution are required (Dolag et al. 2005; Dolag & Stasyszyn 2009; Donnert et al. 2013; Stasyszyn et al. 2013).

Few papers address the magnetic field amplification in filaments. Early MHD grid simulations by Sigl, Miniati & Ensslin (2003) predicted  $\sim 10\text{--}100$  nG fields in filaments. However, the total normalization of the magnetic fields had to be scaled up in order to match the observation of the Coma cluster. Taking this into account and normalizing by the assumed initial seed field, these simulations essentially showed only compressive amplification of magnetic fields in filaments, in line with what we also find at low resolution. Brüggen et al. (2005) applied instead AMR and a passive scheme in FLASH to monitor the amplification of magnetic fields also at the scale of filaments, and reported an average amplification factor of  $\sim 10^3\text{--}10^4$  for the magnetic energy of filaments, i.e. larger than what we found here. This can be explained by the difference in the adopted MHD scheme, even if the spectra of magnetic fields did not show evidence for small-scale dynamo amplification and the topology of magnetic fields in filaments was found to be laminar.

Smaller amplification factors for the magnetic energy, essentially in agreement with our results here, were found using SPH simulations by Dolag et al. (2004) with a constrained realization of the nearby (100 Mpc)<sup>3</sup> Universe. Finally, several of our results have already been explained by Ryu et al. (2008), who used a hybrid approach to rescale the magnetic field distribution obtained with a passive MHD solver coupled to a cosmological simulations. In post-processing, they then estimated the saturated growth of magnetic fields based on the (unresolved) turbulent decay of vortical motions resolved in the simulation. The important difference in the modes of turbulent forcing in filaments and galaxy clusters, and its impact on the amplification of weak primordial fields was already pointed out in their work, and our direct simulation with a larger spatial resolution confirmed their main results (Ryu et al. 2008). However, our simulations (see also our tests in the appendix) have shown that the results of dynamo amplification in driven turbulence (specially in the isothermal case) cannot be trusted to exactly predict the maximum dynamo amplification in WHIM. First, due to the major role played by shocks even in the filament interiors, which cannot be fully captured with isothermal computations, since this largely underestimates the role of the baroclinic generation of vorticity. And, secondly, because of the presence of strong longitudinal motions along the filament that prevents the continuous build-up of small-scale magnetic field at any specify location within the filament, as instead observed at the centre of clusters.

## 5 CONCLUSIONS

We have studied the amplification of primordial magnetic fields via a small-scale turbulent dynamo using direct MHD numerical simulations with ENZO (Wang & Abel 2009; Wang et al. 2010; Bryan G. L. et al. (The Enzo Collaboration), 2014). In particular, we have investigated the amplification of magnetic fields in the ICM and

in the WHIM of filaments. While in the ICM we confirm that turbulence from structure formation can produce significant dynamo amplification (even if the measured efficiency is smaller than what is reported in some papers), in filaments we do not observe significant dynamo amplification, even though we reached Reynolds numbers of  $R_e \sim 200$ . The maximum amplification for large filaments is of the order of  $\sim 100$  for the magnetic energy, mostly due to strong compression in supersonic flows, corresponding to a typical field of a few  $\sim$ nG. This result is independent of resolution and follows from the inefficiency of supersonic motions in the WHIM in triggering solenoidal modes, while compressive modes are dominant in filaments at all investigated resolutions.

Our results can serve as a guideline for the minimum resolution for the onset of small-scale dynamo in cosmological simulations. Our results for the ICM (Section 3.1) suggest that a dynamical range of at least  $L/\Delta x \sim 210$  (where  $L$  is the scale for the driving of turbulence and  $\Delta x$  is the numerical resolution) is necessary to observe the build-up of small-scale magnetic field in a dynamo process, as this would enable a flow with  $R_e \geq 500$ . Even if the bulk of turbulence injection in the ICM at late redshift happens through mergers and on scales of a fraction of the virial radius (Vazza et al. 2009, 2011b, 2012), the converging accretion flows within and the injection of vorticity at accretion shocks (Ryu et al. 2008; Miniati 2014) are likely to build up magnetic fields in the ICM on scales up to the order of the virial radius. Assuming  $L \approx 2R_v$ , the above criterion suggests that  $\Delta x/R_v \leq 100$  to have efficient dynamo, i.e. in order to achieve a large enough Reynolds number for small-scale dynamo, a cosmological simulation needs a spatial resolution of the order of  $\sim 30$  kpc for a  $10^{15} M_\odot$  halo ( $R_v \approx 3$  Mpc), of the order of  $\sim 10$  kpc for a  $10^{14} M_\odot$  halo, and of the order of  $\sim 3$  kpc for  $10^{13} M_\odot$ . The fact that clusters form late, combined with the fact that mergers typical inject energy at scales below  $R_v$ , likely makes the above estimate a lower limit on the required resolution, as shown in our larger cosmological run (Section 3.3).

It is more difficult to draw firm conclusions in the case of filaments, as our runs do not clearly show a convergence on the dynamo process. Our results suggest that a dynamical resolution equal or larger than  $L/\Delta x \sim 60$  (where  $L$  is the width of the filament) is necessary to approach convergence in the energy share of solenoidal and compressive motions (Fig. 17), which sets the nature of the turbulent forcing within the system. Despite the fact that the theoretical Reynolds number available to the flow is large,  $R_e \geq 10^2$ , in the presence of this dominant compressive forcing no clear evidence of a fast dynamo is detected, even in our highest resolution runs, where the total magnetic energy is only  $\sim 10^{-5}$  of the kinetic energy and carries memory of the initial magnetic field imposed at  $z = 30$ .

The observational consequences of these results are important. First, the deflection of UHECRs by filaments in the cosmic web is expected to be fairly small, i.e.  $\leq 1$  deg, allowing the identification of extragalactic sources (Sigl et al. 2003; Ryu et al. 2010). Secondly, the detection of synchrotron emission by electrons accelerated by shocks surrounding filaments will be very challenging since diffusive shock acceleration requires a minimum magnetic field of  $\sim 0.05\text{--}0.1\mu\text{G}$  (Vazza et al., submitted). Within the present uncertainties about the magnetization level of the WHIM, we suggest that *any* observation of large-scale fields in filaments in the radio band will contain valuable information about the strength of primordial magnetic fields (e.g. Neronov & Vovk 2010; Widrow et al. 2012). Since the growth of primordial magnetic fields in filaments should be dominated by simple compression and small-scale shocks, the dynamical memory of the system should persist over

long cosmological times, and any observed magnetization level should closely connect to the primordial magnetization. This is different from galaxy clusters where most of the magnetic energy is extracted from the kinetic energy budget, thereby quickly erasing previous dynamical information.

Finally, we stress that our results imply by no means that the quest for higher resolution in the filamentary structures of the cosmic web is useless. Provided that MHD can still be applied there (Section 4), resolution can significantly impact the Faraday rotation from the Intra Galactic Medium (IGM), which the SKA might probe (e.g. Akahori, Gaensler & Ryu 2014). It also affects the synchrotron emission from the cosmic web (Brown 2011; Araya-Melo et al. 2012) because shock statistics change with resolution (Vazza et al. 2011a). The use of high resolution also allows us to model galaxy formation processes in filamentary environments in detail, which is crucial to study the impact of magnetized outflows from galaxies (Xu et al. 2009; Donnert et al. 2009; Beck et al. 2013).

## ACKNOWLEDGEMENTS

Computations described in this work were performed using the ENZO code (<http://enzo-project.org>), which is the product of a collaborative effort of scientists at many universities and national laboratories. We gratefully acknowledge the ENZO development group for providing extremely helpful and well-maintained online documentation and tutorials.

Most of the simulations of these work have been ran on Piz-Daint at CSCS-ETH, under the CHRONOS programme 2014, which we gratefully acknowledge. FV and MB also acknowledge the usage of computational resources on the JUROPA cluster at the Juelich Supercomputing Centre (JSC), under project no. 5018 and 7006. FV and MB acknowledge support from the grant FOR1254 from the Deutsche Forschungsgemeinschaft. We thankfully acknowledge J. Donnert, D. Schleicher, M. A. Latif, K. Subramanian and F. Miniati for very fruitful scientific discussion. We thank L. Vazza for his late but fundamental reading of the manuscript.

## REFERENCES

Akahori T., Gaensler B. M., Ryu D., 2014, *ApJ*, 790, 123

Alves Batista R., Schiffer P., Sigl G., 2014, *Nucl. Instrum. Methods Phys. Res. A*, 742, 245

Araya-Melo P. A., Aragón-Calvo M. A., Brüggen M., Hoeft M., 2012, *MNRAS*, 423, 2325

Bauer A., Springel V., 2012, *MNRAS*, 423, 2558

Beck R., Brandenburg A., Moss D., Shukurov A., Sokoloff D., 1996, *ARA&A*, 34, 155

Beck A. M., Lesch H., Dolag K., Kotarba H., Geng A., Stasyszyn F. A., 2012, *MNRAS*, 422, 2152

Beck A. M., Dolag K., Lesch H., Kronberg P. P., 2013, *MNRAS*, 435, 3575

Bhat P., Subramanian K., 2013, *MNRAS*, 429, 2469

Bonafede A., Feretti L., Murgia M., Govoni F., Giovannini G., Dallacasa D., Dolag K., Taylor G. B., 2010, *A&A*, 513, A30

Bonafede A., Dolag K., Stasyszyn F., Murante G., Borgani S., 2011, *MNRAS*, 418, 2234

Bonafede A., Vazza F., Brüggen M., Murgia M., Govoni F., Feretti L., Giovannini G., Ogrean G., 2013, *MNRAS*, 433, 3208

Brown S. D., 2011, *J. Astrophys. Astron.*, 32, 577

Brüggen M., 2013, *MNRAS*, 436, 294

Brüggen M., Ruszkowski M., Simionescu A., Hoeft M., Dalla Vecchia C., 2005, *ApJ*, 631, L21

Brüggen M., Bykov A., Ryu D., Röttgering H., 2011, *Space Sci. Rev.*, 71

Brunetti G., Lazarian A., 2011, *MNRAS*, 412, 817

Bryan G. L. et al. (The Enzo Collaboration), 2014, *ApJS*, 211, 19

Cautun M., van de Weygaert R., Jones B. J. T., Frenk C. S., 2014, *MNRAS*, 441, 2923

Cho J., Vishniac E. T., Beresnyak A., Lazarian A., Ryu D., 2009, *ApJ*, 693, 1449

Collins D. C., Xu H., Norman M. L., Li H., Li S., 2010, *ApJS*, 186, 308

Dedner A., Kemm F., Kröner D., Munz C.-D., Schnitzer T., Wesenberg M., 2002, *J. Comput. Phys.*, 175, 645

Dolag K., Stasyszyn F., 2009, *MNRAS*, 398, 1678

Dolag K., Bartelmann M., Lesch H., 1999, *A&A*, 348, 351

Dolag K., Grasso D., Springel V., Tkachev I., 2004, *Sov. J. Exp. Theor. Phys. Lett.*, 79, 583

Dolag K., Vazza F., Brunetti G., Tormen G., 2005, *MNRAS*, 364, 753

Dolag K., Bykov A. M., Diaferio A., 2008, *Space Sci. Rev.*, 134, 311

Donnert J., Dolag K., Lesch H., Müller E., 2009, *MNRAS*, 392, 1008

Donnert J., Dolag K., Brunetti G., Cassano R., 2013, *MNRAS*, 429, 3564

Drury L. O., Downes T. P., 2012, *MNRAS*, 427, 2308

Dubois Y., Teyssier R., 2008, *A&A*, 482, L13

Federrath C., Chabrier G., Schober J., Banerjee R., Klessen R. S., Schleicher D. R. G., 2011a, *Phys. Rev. Lett.*, 107, 114504

Federrath C., Sur S., Schleicher D. R. G., Banerjee R., Klessen R. S., 2011b, *ApJ*, 731, 62

Ferrari C., Govoni F., Schindler S., Bykov A. M., Rephaeli Y., 2008, *Space Sci. Rev.*, 134, 93

Gaspari M., Churazov E., 2013, *A&A*, 559, A78

Gazzola L., King E. J., Pearce F. R., Coles P., 2007, *MNRAS*, 375, 657

Harten A., Hyman J. M., 1983, *JCoPh*, 50, 235

Haugen N. E. L., Brandenburg A., 2006, *Phys. Fluids*, 18, 075106

Haugen N. E. L., Brandenburg A., Dobler W., 2003, *ApJ*, 597, L141

Iapichino L., Schmidt W., Niemeyer J. C., Merklein J., 2011, *MNRAS*, 414, 2297

Jones T. W., Porter D. H., Ryu D., Cho J., 2011, preprint ([arXiv: e-prints](http://arXiv.org/abs/1108.0205))

Komatsu E. et al., 2011, *ApJS*, 192, 18

Kritsuk A. G. et al., 2011, *ApJ*, 737, 13

Kronberg P. P., Lesch H., Hopp U., 1999, *ApJ*, 511, 56

Kronberg P. P., Bernet M. L., Miniati F., Lilly S. J., Short M. B., Higdon D. M., 2008, *ApJ*, 676, 70

Kulsrud R. M., Cen R., Ostriker J. P., Ryu D., 1997, *ApJ*, 480, 481

Kunz M. W., Schekochihin A. A., Cowley S. C., Binney J. J., Sanders J. S., 2011, *MNRAS*, 410, 2446

Latif M. A., Schleicher D. R. G., Schmidt W., Niemeyer J., 2013, *MNRAS*, 432, 668

Mao S. A. et al., 2012, *ApJ*, 755, 21

Mignone A., Tzeferacos P., Bodo G., 2010, *J. Comput. Phys.*, 229, 5896

Miniati F., 2014, *ApJ*, 782, 21

Murgia M., Govoni F., Feretti L., Giovannini G., Dallacasa D., Fanti R., Taylor G. B., Dolag K., 2004, *A&A*, 424, 429

Neronov A., Vovk I., 2010, *Science*, 328, 73

Pakmor R., Marinacci F., Springel V., 2014, *ApJ*, 783, L20

Parrish I. J., Stone J. M., Lemaster N., 2008, *ApJ*, 688, 905

Price D. J., 2012, *MNRAS*, 420, L33

Ruszkowski M., Lee D., Brüggen M., Parrish I., Oh S. P., 2011, *ApJ*, 740, 81

Ryu D., Kang H., Cho J., Das S., 2008, *Science*, 320, 909

Ryu D., Das S., Kang H., 2010, *ApJ*, 710, 1422

Ryu D., Schleicher D. R. G., Treumann R. A., Tsagas C. G., Widrow L. M., 2012, *SSRv*, 166, 1

Schekochihin A. A., Cowley S. C., Taylor S. F., Maron J. L., McWilliams J. C., 2004, *ApJ*, 612, 276

Schekochihin A. A., Cowley S. C., Kulsrud R. M., Hammett G. W., Sharma P., 2005, *ApJ*, 629, 139

Schleicher D. R. G., Beck R., 2013, *A&A*, 556, A142

Schleicher D. R. G., Schober J., Federrath C., Bovino S., Schmidt W., 2013, *New J. Phys.*, 15, 023017

Schlickeiser R., 2012, *Phys. Rev. Lett.*, 109, 261101

Schober J., Schleicher D., Federrath C., Klessen R., Banerjee R., 2012, *Phys. Rev. E*, 85, 026303

Schober J., Schleicher D. R. G., Klessen R. S., 2013, *A&A*, 560, A87

Shu C.-W., Osher S., 1988, *J. Comput. Phys.*, 77, 439  
 Sigl G., Miniati F., Ensslin T. A., 2003, *Phys. Rev. D*, 68, 043002  
 Skillman S. W., Xu H., Hallman E. J., O’Shea B. W., Burns J. O., Li H.,  
 Collins D. C., Norman M. L., 2013, *ApJ*, 765, 21  
 Stasyszyn F. A., Dolag K., Beck A. M., 2013, *MNRAS*, 428, 13  
 Subramanian K., Shukurov A., Haugen N. E. L., 2006, *MNRAS*, 366, 1437  
 Turk M. J., Oishi J. S., Abel T., Bryan G. L., 2012, *ApJ*, 745, 154  
 Vazza F., Brunetti G., Kritsuk A., Wagner R., Gheller C., Norman M., 2009,  
*A&A*, 504, 33  
 Vazza F., Dolag K., Ryu D., Brunetti G., Gheller C., Kang H., Pfrommer C.,  
 2011a, *MNRAS*, 418, 960  
 Vazza F., Brunetti G., Gheller C., Brunino R., Brüggen M., 2011b, *A&A*,  
 529, A17  
 Vazza F., Roediger E., Brueggen M., 2012, *A&A*, 544, A103  
 Völk H. J., Atoyan A. M., 2000, *ApJ*, 541, 88  
 Wang P., Abel T., 2009, *ApJ*, 696, 96  
 Wang P., Abel T., Kaehler R., 2010, *New Astron.*, 15, 581  
 Weinberg M. D., 2014, *MNRAS*, 438, 2995  
 Widrow L. M., Ryu D., Schleicher D. R. G., Subramanian K., Tsagas C. G.,  
 Treumann R. A., 2012, *SSRv*, 166, 37  
 Xu H., Li H., Collins D. C., Li S., Norman M. L., 2009, *ApJ*, 698, L14  
 Xu H., Li H., Collins D. C., Li S., Norman M. L., 2011, *ApJ*, 739, 77  
 Zhu W., Feng L.-l., Xia Y., Shu C.-W., Gu Q., Fang L.-Z., 2013, *ApJ*, 777, 48

## APPENDIX A: TESTS OF TURBULENCE IN A BOX

In this appendix, we show results from simulations of dynamo amplification in driven turbulence with ENZO. A thorough analysis of driven turbulence experiments has been given by (Schekochihin et al. 2004; Ryu et al. 2008; Cho et al. 2009; Federrath et al. 2011a; Jones et al. 2011). Our runs serve as a proof of concept for small-scale dynamo in flows with large numerical Reynolds number, and as a preliminary benchmark for the application of the ENZO-MHD algorithm to larger cosmological simulations.

In detail, we simulated the evolution of MHD turbulence in a regular box starting with uniform density, temperature and passive uniform magnetic fields, equation of state  $\gamma = 5/3$ , and applied continuous stirring from turbulence injected at  $k = 2$  (where  $k = 1$  corresponds to the box size). This is done with a specific module available in ENZO, that generates random isotropic velocity fields with specified input spectra and absolute normalization for the total velocity field (Wang et al. 2010).

In our tests, we employed  $512^3$  boxes and drove  $M = 1.5$  and 15 isotropic motions in a continuous way. Fig. A1 shows the magnetic field strength at three different times for these two runs, at epochs  $\approx 0.005t_{\text{dyn}}$ ,  $\approx 1.5t_{\text{dyn}}$ , and  $\approx 3t_{\text{dyn}}$ , where the dynamical times is defined as  $t_{\text{dyn}} = L_{\text{box}}/V_{\text{drive}}$  ( $L_{\text{box}}$  is the box size and  $V_{\text{drive}} = Mc_s$  is the rms velocity at the forcing scale).

The evolution of kinetic and magnetic spectra until  $4t_{\text{dyn}}$  for the two cases is given in Fig. A2, and highlights the significantly different evolution of magnetic field structure in the two regimes. In the  $M = 15$  case after a very tiny fraction ( $10^{-2}$ ) of the dynamic time, we see the emergence of magnetic energy on very small scales, as an effect of shocks that are formed very early inside the box due to strong supersonic motions. The small-scale magnetic energy increases over time, without significantly changing the location of the peak of magnetic energy, and after  $\sim 4t_{\text{dyn}}$ , we observe the hint of equipartition with kinetic energy on the smallest scales. This case is close to the case of the WHIM in cosmic filaments, due to the involved supersonic flow, even if the multiple collisions of oblique shocks are more efficient in driving solenoidal motions in the medium (mostly through baroclinic generation of vorticity and

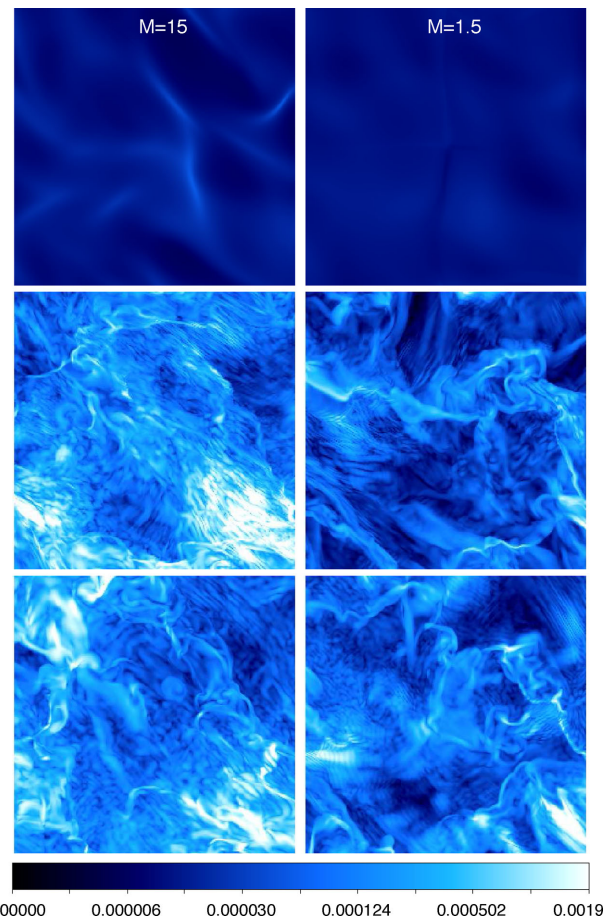


**Figure A1.** Maps of magnetic field strength (arbitrary units) for a central slice in our driven turbulence tests with  $512^3$ , for the  $M = 15$  forcing (left) and the  $M = 1.5$  forcing (right) case, at the epochs of  $\approx 0.005t_{\text{dyn}}$ ,  $\approx 1.5t_{\text{dyn}}$ , and  $\approx 3t_{\text{dyn}}$ , where  $t_{\text{dyn}}$  is the dynamical time.

at curved shocks through Crocco’s theorem, e.g. Jones et al. 2011), which reaches roughly an  $\sim 50$  per cent budget of the total kinetic energy at the end of the run, i.e. much more than in our simulated filament. Moreover, the forcing to which the magnetic eddies are subjected is constant in time, while in the case of filaments (Section 3.2) strong advection motions longitudinal to the major axis of the filament tend to continuously replace magnetic eddies at a given Eulerian location, thereby reducing their growth rate.

Conversely, the  $M = 1.5$  is closer to the case of the simulated ICM, given the transonic forcing regime and the enhanced presence of solenoidal motions by the end of the run ( $\sim 60$ ) per cent of the total kinetic energy, i.e. similar to our high-resolution ICM runs. In this case, we observe in the spectra a slower build-up of small-scale magnetic energy, and the progressive increase of the total velocity spectrum over time. In this transonic forcing the thermalization of kinetic energy at shocks is obviously greatly reduced, and a more volume filling and tangled velocity field can build over time. Roughly after one dynamical time, we observe the formation of a well-defined peak in the magnetic spectrum, that progressively moves to larger spatial scales and becomes of the same order the kinetic energy at the smallest scales, as predicted in efficient small-scale dynamo (Schekochihin et al. 2004; Cho et al. 2009).

Both simulations confirm the possibility of simulating small-scale dynamo amplification with the ENZO-MHD version we adopted to

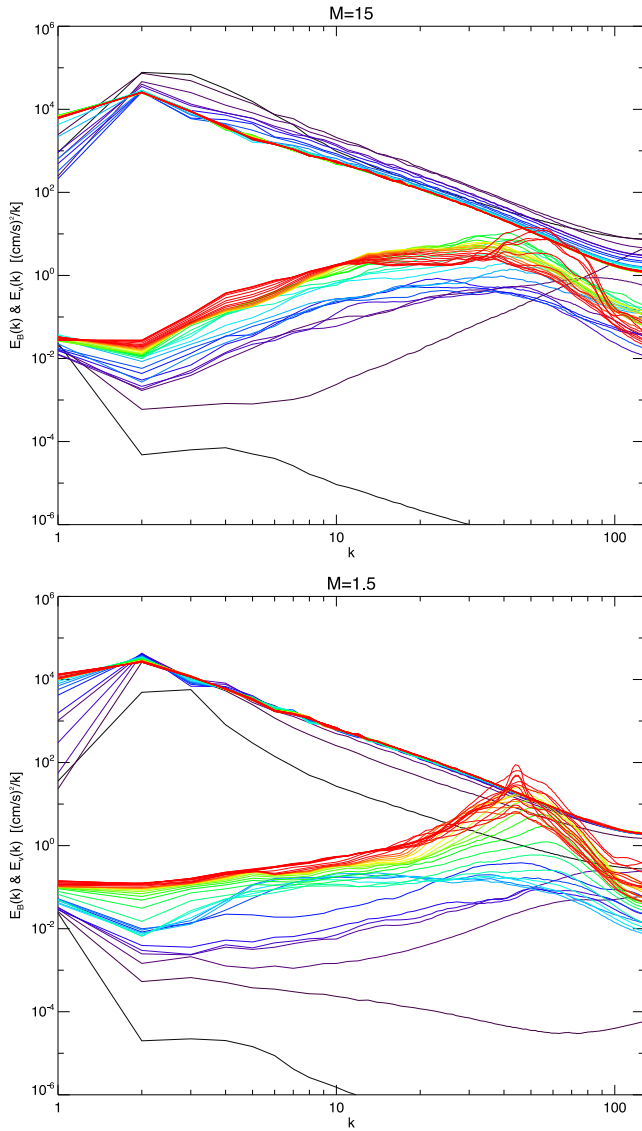


**Figure A2.** Velocity power spectra (solid lines) and magnetic power spectra (dot-dashed lines) for two  $512^3$  ‘turbulence in a box’ runs, assuming a constant forcing of  $M = 15$  (left) and of  $M = 1.5$  (right). All spectra are computed within a  $256^3$  subvolume contained in the two boxes. The time evolution samples  $\sim 4t_{\text{dyn}}$  with roughly constant time spacing.

obtain our results in the main paper, and suggest that to get to more quantitative answers in the case of the ICM and of the WHIM one must resort to proper 3D cosmological simulation, in order to have the large-scale dynamics properly taken into account.